The Pennsylvania State University

The Graduate School

Department of Electrical Engineering

OPTICAL DESIGN FOR ADVANCED LIDAR DETECTORS

A Thesis in

Electrical Engineering

by

Ginnipal S. Chadha

Submitted in Partial Fulfillment
of the Requirements
for the Degree of

Master of Science

May 2001

We approve the thesis of Ginnipal S.Chadha.

Date of Signature

_____ _____

C. Russell Philbrick
Professor of Electrical Engineering
Thesis Advisor

_____ _____

Sven Bilén
Assistant Professor of Electrical Engineering

_____ _____

Kenneth Jenkins
Professor of Electrical Engineering
Head of the Department of Electrical Engineering

Abstract

A **LI**ght **D**etection **A**nd **R**anging system, commonly referred to as lidar, transmits a laser beam at a certain wavelength into the atmosphere, and a telescope collects the return signals, including direct backscatter, vibrational Raman, and rotational Raman signals at different wavelengths. The return signals are then detected to obtain measurements of atmospheric properties. The potential use of lidar instruments as a replacement for current remote sensing technologies have fueled efforts to develop accurate, high resolution and autonomous lidar instruments. The Lidar Atmospheric Profile Sensor (LAPS) unit is a unique optical remote sensing instrument which was developed at Penn State University for the US Navy. It is used in the study of atmospheric properties and constituents using the technique of molecular Raman scattering. Experience with operating the LAPS instrument over a number of campaigns has highlighted design and performance benefits that could be gained from revisiting the original LAPS detector design. ALAPS (Advanced Lidar Atmospheric Profile Sensor), which is an advanced version of the LAPS instrument being developed as a commercial prototype at Penn State University, will benefit from the new designs developed for the advanced detector reported here. The optical paths in the LAPS detector and the advanced detector were investigated using optical simulation software called ZEMAX. Using the simulated performance we can determine the beam spot size and the location where lens should be placed relative to the fiber to obtain the best results over the wide range of wavelengths. The effects of aberrations and alignment errors that cause vignetting can be minimized or eliminated to arrive at a more efficient optical design. The advanced detector design aims

to eliminate the uncertainties in measurements which have been identified with the LAPS instrument and also provide a commercially viable design. The advanced design incorporates a self-calibration mechanism using a filter-switching slide, which will be used to calibrate the instrument and monitor performance by measuring the relative transmission and efficiency of the channels. The new detector system, incorporates higher speed photomultiplier tubes (PMTs) and faster electronics to increase the data resolution from 75 m (500 ns) to 3 m (20 ns). The optical design includes the analysis of the new detector and testing to improve performance of the present LAPS detector. The detector design has been prepared to provide capability for self-calibration and for monitoring of detector performance, and it has been verified using simulations and experimental results.

Table of Contents

List of Figures

List of Tables

Acknowledgments

These past years have proved to be defining in pursuit of my career objectives. I would like to thank my advisor, Professor C. Russell Philbrick, for fueling my interest in the field of Optics and its applications. His commitment to work is inspiring and his guidance and encouragement helped keep me focused in my efforts. I would also like to thank Dr. Sven Bilén, for taking an active interest in my research. His suggestions were very helpful.

Thanks are also due to Alex Achey, Gregg O'Marr, Ed Novitsky, Homer Li, Corey Slick, Sriram Kizhakkemadam, Prarthana Pai, Karoline Mulik and other students who worked in development of the lidar instrument over these years.

I would also like to take this opportunity to thank my parents and sisters for their support and encouragement, and Kiran, for her patience and understanding. My achievements mean all the more because of them.

Chapter 1

Introduction

The development and refinement of sophisticated optical remote sensing techniques during the past decade have contributed enormously to our knowledge about the atmosphere. Optical remote sensing provides a meaningful method of studying the temporal and spatial variations of the atmosphere and its constituents using elastic and inelastic scattering of light. The remote sensing instrument utilized in these studies is LIght Detection And Ranging (lidar), which is a radar at optical wavelengths. Lidar has demonstrated capabilities to profile all of the major properties of the lower atmosphere. Lidar provides an important means of measuring atmospheric properties because it has the capability of continuous, autonomous measurement and provides time sequence profiles used to describe the vertical and horizontal structure of the lower atmosphere. Raman lidar techniques use a laser at a certain wavelength to transmit an intense pulse of optical radiation and then measure the Raman-shifted backscatter of photons from molecules. Raman inelastic scattering occurs when laser radiation is scattered by molecules at energy differences associated with the vibrational and rotational energy states of the molecules. The wavelength shift of the scattered radiation is due to the energy difference between the vibrational and rotational states. Active optical remote sensing techniques based on lidar have been limited in the past to ground-based and aircraft applications due to size and performance restrictions. The advances in electro-optical components have encouraged efforts to advance ground measurement capabilities with a view towards future compact lidar systems to serve a wider range of applications

[Philbrick et al., 1996]. Current ground based lidar systems have successfully provided profiling of atmospheric constituents such as temperature, water vapor, refractivity, density, chemical species, aerosol extinction and particle characteristics [Philbrick et al., 1996]. The manufacture of reliable and stable lasers, development of measurement techniques, and availability of highly efficient optical components have further enhanced these capabilities. The potential use of lidar instruments to replace balloon technniques employing expendable hardware has fueled efforts to develop accurate, high resolution and autonomous lidar instruments. Such instruments improve the spatial and temporal resolution and decrease the costs for profiling atmospheric properties.

The LAPS (Lidar Atmospheric Profile Sensor) instrument was the fifth in a series of lidar instruments developed to advance the capability to obtain atmospheric profile data. It was originally designed as a rugged prototype instrument for the U.S. Navy to obtain RF refractivity measurements in a shipboard environment [Philbrick, 1994]. The instrument was completed in mid-1996 and has been deployed for a number of scientific investigations following its demonstration for the US Navy aboard the *USNS Sumner* during August-October, 1996. Its capabilities and accuracy in providing atmospheric data has been the subject of a number of technical papers and comparative studies with other sources of data [Philbrick, 1998a]. Work is currently underway to develop the Advanced LAPS (ALAPS) instrument, which will serve as an engineering prototype for commercial production of lidar instruments.

The focus of my research efforts has been to optimize the optical detector for the Raman return signals. The first step was to understand the limitations of the LAPS instrument by evaluating available data sets from past campaigns and by revisiting the

optical design. A self-calibration scheme for lidar measurements is proposed that will eliminate the dependence on independent sources of data to determine and verify the instrument sensitivity. The design has been verified using computer simulation and experimental results. This thesis is organized in sections beginning with a description of the LAPS detector and receiver system. The proposed optical detector design eliminates the limitations found in the LAPS detector. The aim of this thesis is to serve as a comprehensive documentation for the detector design of the advanced instrument. Mechanical and optical designs for the detector are proposed. The benefits, performance expectations, and future work required to demonstrate the capabilities of the advanced detector are described.

CHAPTER 2

Lidar Atmospheric Profile Sensor (LAPS) Instrument

2.1 Introduction to LAPS

The Lidar Atmospheric Profile Sensor (LAPS) unit is an optical remote sensing instrument for investigations of the atmosphere and its constituents using the property of molecular Raman scattering. The LAPS instrument transmits laser beams at 266 nm and 532 nm into the atmosphere, and a telescope collects the return signals, including direct backscatter, vibrational Raman and rotational Raman signals at several wavelengths. The return signals are then detected and processed to obtain measurements of atmospheric structure and constituents. The intensity of a vibrational Raman signal is directly proportional to the density of the scattering molecules and independent of other molecular species. The wavelength shift and narrow spectral width of the Raman return signal allows it to be distinguished from solar background radiation and other sources of elastically scattered radiation [Measures, 1984]. The LAPS instrument, a multi-wavelength Raman lidar, was originally designed as a prototype for the U.S. Navy to obtain RF refractivity measurements in a shipboard environment. The LAPS instrument consists of a console and a deck unit, which are connected by fiber optic cables [Balsiger et al., 1996; Jenness et al., 1997]. The main components of the deck unit are a Nd:YAG laser, beam expander telescope, the collecting telescope, and the fiber optic link [Philbrick, 1998]. The Nd:YAG laser is pulsed at 30 Hz with an output power of 1.6 joules per pulse at the fundamental wavelength, 1064.1 nm. The 1064.1-nm laser beam is sent through two frequency-doubling harmonic crystals to transmit at wavelengths of 532

nm (2^{nd} harmonic) and 266 nm (4^{th} harmonic). The radiation at these two wavelengths is scattered by molecules in the atmosphere. The output energy of the laser is not eye-safe, so several safety precautions must be taken during operation. A radar with a six-degree cone angle around the vertical laser beam is used to detect aircraft and send a signal to shut off the beam if detection occurs. The transmission system characteristics of LAPS are given in Table 2.1 [Durbin, 1997; Philbrick, 1998].

Table 2.1. LAPS transmitter characteristics

Laser	Continuum Model 9030 with 5X Beam Expander
Pulse Repetition Frequency	30 Hz
Pulse Duration	8 ns
Fundamental Power	1.6 J/Pulse
Power Output at 1064 nm	Dumped into heat sink
Power Output at 532 nm	600 mJ
Power Output at 266 nm	120 mJ

The return signal is reflected and focused into a 1-mm fiber at the prime focus of a parabolic mirror telescope. The LAPS transmitter and receiver system configuration is shown in Figure 2.1 [Durbin, 1997; Jenness et al., 1997]. The return signal is then transferred by a fiber optic cable to a detector box in the console unit, where the Raman wavelengths are separated and the signal strength measured by the photomultiplier tubes and photon counting electronics. The detector unit and receiver system will be examined in more detail in the subsequent sections.

Figure 2.1. LAPS transmitter and receiver system components [Jenness et al., 1997]

The console provides the control for operation of the instrument, as well as the data collection and display. The original LAPS console contained two PCs, the command computer and the display computer, a data acquisition system, and the detector box. The command computer sends control signals to the deck unit computer for instrument operation and receives signals back that confirm the transmitted control data. The data acquisition system transfers the data signals, as photon counts detected by the PMTs, for processing. LAPS has a vertical resolution of 75 meters for seven of the PMTs and a vertical resolution of 3 meters for the backscatter PMT. The display computer processes the data files on the command computer and further utilizes the lidar scatter equations to display real-time vertical profiles of the water vapor, ozone, temperature, and extinction. Table 2.2 displays a summary of the features of LAPS.

Table 2.2. Summary of LAPS features

Transmitter	Continuum 9030 –30 Hz 5X Beam Expander	600 mJ @ 532 nm 120 mJ @ 266 nm
Receiver	61-cm Diameter Telescope Focal length – 1.5 m	Fiber optic transfer
Detector	Eight PMT channels Photon Counting	660 and 607 nm – Water Vapor 528 and 530 nm – Temperature 295 and 284 nm – Daytime Water Vapor 277 and 284 nm – Raman/DIAL Ozone 607, 530, and 284 nm – Extinction 532 nm – Backscatter
Data System	DSP 100 MHz	75-meter range bins
Safety Radar	Marine R-70 X-Band	Protects 6° cone angle around beam

2.2 Measurement Techniques

The LAPS system uses Raman scattering techniques to measure vertical profiles of aerosol extinction, water vapor, temperature, and ozone. Rotational Raman scatter signals are used to measure temperature, whereas vibrational Raman scattering signals are used to measure profiles of water vapor, ozone, and optical extinction. LAPS is able to detect the Raman shifts of several selected molecules using different channels. The vibrational and rotational Raman signals are measured for the 532-nm transmitted laser wavelength and vibrational Raman signals are measured for the 266-nm transmitted laser wavelength. The raw data obtained in photon counts provides information about the concentrations of N_2 and H_2O for visible and N_2, H_2O and O_2 for ultraviolet wavelengths, at different altitudes. These measurements can be interpreted using the basic lidar

scattering equation and variations of it. The lidar scattering equation can be described by the power of the signal received by a monostatic lidar denoted by $P(\lambda_R,z)$, given by Esposito [1999] and Measures [1984]:

$$P(\lambda_R, z) = E_T(\lambda_T)\xi_T(\lambda_T)\xi_R(\lambda_R)\frac{c\tau}{2}\frac{A}{z^2}\beta(\lambda_T, \lambda_R)\exp\left[-\int_0^z[\alpha(\lambda_T, z') + \alpha(\lambda_R, z')]dz'\right] , \qquad [2.1]$$

where,

z	is the altitude of the volume element where the return signal is scattered,
λ_T	is the wavelength of the laser light transmitted,
λ_R	is the wavelength of the laser light received,
$E_T(\lambda_T)$	is the light energy per laser pulse transmitted at wavelength λ_T,
$\xi_T(\lambda_T)$	is the net optical efficiency at wavelength λ_T of all transmitting devices,
$\xi_R(\lambda_R)$	is the net optical efficiency at wavelength λ_R of all receiving devices,
c	is the speed of light,
τ	is the time duration of the laser pulse,
A	is the area of the receiving telescope,
$\beta(\lambda_T,\lambda_R)$	is the back scattering cross section of the volume scattering element for the laser wavelength λ_T at Raman shifted wavelength λ_R,
$\alpha(\lambda,z')$	is the extinction coefficient at wavelength λ at range z'.

This equation is used to interpret the signal returned in photon counts, so that vertical measurements of atmospheric components can be determined.

The LAPS instrument measures extinction at three different wavelengths using the gradients in molecular profiles [O'Brien et. al., 1998; Li et. al., 2000]. LAPS measures extinction using molecular profiles of Raman-shifted nitrogen at 607 nm resulting from the 532-nm transmitted wavelength and at 284 nm resulting from the 266-nm transmitted wavelength. Another extinction measurement is made by using the rotational Raman signal of nitrogen and oxygen at 530 nm from the 532-nm transmitted wavelength.

Water vapor mixing ratio, also known as specific humidity, is measured at both ultraviolet and visible wavelengths. Ultraviolet channel measurements are made both day and night, while visible channel measurements are only made during the night. Daytime ultraviolet measurements are possible since they are made in the "solar blind" region of the ultraviolet spectrum (200-300 nm). The water vapor mixing ratio is calculated by taking the ratio of the return signal at two different wavelengths, i.e., the 1st Stokes vibrational Raman shifted signal from water divided by that from nitrogen, and multiplying by a calibration factor. The return signal of nitrogen (607 nm for visible channels, 284 nm for ultraviolet channels) is proportional to the density of ambient air. The following equation is used to determine the vertical profiles of water vapor, W(z) [Esposito, 1999],

$$W(z) = K_{cal} \frac{S_{H2O}(z)}{S_{N2}(z)} \qquad [2.2]$$

where,

S_{H2O} is the signal from the vibrational Raman shift of H_2O at 660 or 295 nm,

S_{N2} is the signal from the vibrational Raman shift of N_2 at 607 or 284 nm,

K_{cal} is a calibration constant.

The calibration constant, K_{cal}, is found by fitting the ratio of S_{H2O} to S_{N2} to radiosonde data, or determined from the relative sensitivity of the two channels taken together with the scattering cross-sections.

A DIAL (DIfferential Absorption Lidar) analysis of the Raman signals, shifted by N_2 (284 nm) and O_2 (277 nm), which occur on the steep side of the Hartley absorption band of ozone, is used to obtain ozone measurements. Vertical profiles of ozone are

calculated by taking the ratio of the Raman-shifted O_2 and N_2 signals using the equation [Esposito, 1999]:

$$\frac{P_{O2}(z)}{P_{N2}(z)} = k_{system.} \exp\left[-\int_0^z [\alpha_m(\lambda_{O2,}\, z') - \alpha_m(\lambda_{N2,}\, z')]dz'\right] \exp\left[-\int_0^z [\alpha_{O3}(\lambda_{O2,}\, z') - \alpha_{O3}(\lambda_{N2,}\, z')]dz'\right], \quad [2.3]$$

where,

$\alpha_m(\lambda_x,z')$ is the attenuation due to molecular scattering at wavelength λ_x,

$\alpha_{O3}(\lambda_x,z')$ is the attenuation due to ozone absorption at wavelength λ_x,

k_{system} is a constant used for simplification, given by:

$$k_{system} = \frac{\xi_R(\lambda_{O2})}{\xi_R(\lambda_{N2})} \frac{\sigma_{O2}}{\sigma_{N2}} \frac{N_{O2}(z)}{N_{N2}(z)} \quad [2.4]$$

The LAPS instrument measures temperature by taking the ratio of the rotational Raman scatter signals due to N_2 and O_2 at 530 nm and 528 nm. The ratio of the 530 nm and 528 nm signals must be fitted to radiosonde balloon data for calibration [Harris, 1995]. The fit is performed using a least squares method using the following equation:

$$T(R) = aR^2 + bR + c \quad , \quad [2.5]$$

where,

T(R) is the temperature as a function of the lidar signal ratio,

R is the lidar ratio of the 530-nm signal and the 528-nm signal,

a, *b*, and *c* are calibration constants determined from filter sonde data.

Vertical profiles of backscatter from airborne particles are measured using a detector with a filter centered at the transmitted wavelength of 532 nm. The backscatter detector is a photon-counting PMT that was added to the LAPS instrument in 1999. This

PMT uses faster electronics to provide a resolution of 3 meters, whereas the seven other PMTs have a resolution of 75 meters due to the 500-ns data bins.

2.3 LAPS detector system

The return signal is transferred by a multimode Step Index (SI) fiber optic cable to a detector box in the console unit. The diverging beam from the fiber is collimated using a 38-mm focal length plano-convex lens. The lens material must have high transmission through both visible and the UV wavelengths. For this reason, we have chosen a UV-grade fused-silica lens. A dichroic beam splitter positioned at 45 degrees to the beam reflects the UV wavelengths and allows the visible to pass through (see Figure 2.2). These beams are further separated into individual bands using wavelength dependent beam splitters which direct the signals to the respective narrow band-pass filters. Seven of the filters were selected at the vibrational and rotational Raman-shifted wavelengths for the two transmitted wavelengths (see Table 2.2), and in addition a filter centered at 532 nm to detect the backscatter signal. Narrow band filter performance requires a collimated beam to minimize the shifting of the center wavelength to shorter wavelengths, and to prevent widening of the pass-band. Because Raman scatter cross-sections are small, the scattered photons are few in number, and high-sensitivity photomultiplier tubes in photon-counting mode are used for detection. For optimal detection performance of the Raman signals, the PMTs should have high collection efficiency, high gain, good multiplication statistics, low noise, and high photocathode quantum efficiency in the spectral range of interest. Table 2.3 lists the optical elements used in the LAPS detector with the numbers referring to the elements in Figure 2.2. Table

2.4 lists the transmission, reflection and efficiency factors of the optical elements in each channel. The total detector efficiency is computed by multiplying these factors for each channel. The total efficiency is expressed as a percentage of the total number of photons counted by the photomultiplier tube to the total number of photons incident on the mirror surface for that wavelength. The total efficiency computed in Table 2.4 would be valid for altitudes above 800 m. Below 800 m the efficiency varies because of the collection function of the telescope form factor.

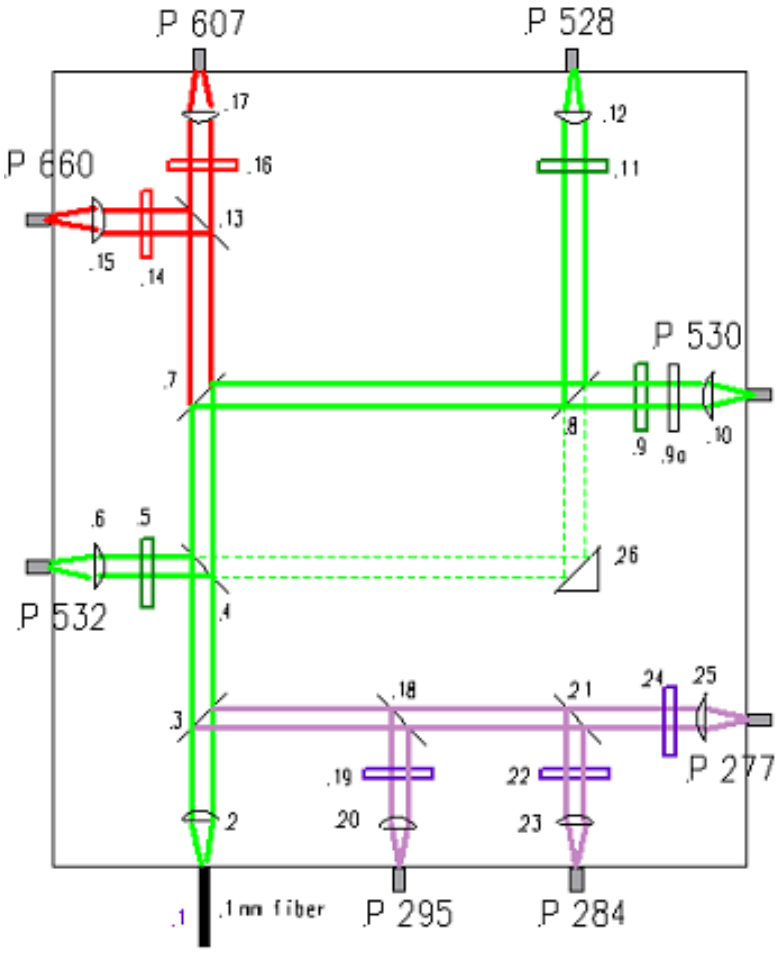

Figure 2.2. Optical element layout for LAPS detector.

Table 2.3. List of optical components, as referred to Figure 2.2

Ref. #	Description
1	Superguide G All–Silica SFS fiber, NA=0.22,1-mm dia core
2	Fused Silica plano-convex lens, 25 mm f, 12.7 mm dia, wideband AR coated
3	Beamsplitter R: 277, 283, 294 nm T: 532, 528, 530, 607, 660 nm
4*	Beam Splitter R: 1% T: 99%
5	Metal Oxide narrow band filter, CWL=532 nm FWHM=0.7 nm,1" dia
6	Fused Silica plano-convex lens, 75 mm f, 1" dia
7	Beamsplitter R: 532, 528, 530 nm T: 660, 607 nm
8	Beamsplitter R:70% T:30%, wideband
9	2 Metal Oxide narrow band filters, CWL=530 nm, FWHM=0.7 nm,1" dia each
9a	2 OD filters, T 50% each
10	Fused Silica plano-convex lens, 75 mm f, 1" dia
11	2 Metal Oxide narrow band filter, CWL=528 nm FWHM=0.7 nm,1" dia each
12	Fused Silica plano-convex lens, 75 mm f, 1" dia
13	Beamsplitter R: 660 nm T: 607 nm
14	Metal Oxide narrow band filter, CWL=660.3 nm, FWHM=0.35 nm,1" dia
15	Fused Silica plano-convex lens, 75 mm f, 1" dia
16	Metal Oxide narrow band filter, CWL=607.3 nm FWHM=0.35 nm,1" dia
17	Fused Silica plano-convex lens, 75 mm f, 1" dia
18	Beamsplitter R: 294 nm T: 283, 277 nm
19	Metal Oxide narrow band filter, CWL=294.7 nm FWHM= 5 nm,1" dia
20	Fused Silica plano-convex lens, 75 mm f, 1" dia
21	Beamsplitter R: 283 nm T: 277 nm
22	Metal Oxide narrow band filter, CWL=283.6 nm FWHM= 5 nm,1" dia
23	Fused Silica plano-convex lens, 75 mm f, 1" dia
24	Metal Oxide narrow band filter, CWL=277.5 nm FWHM= 3 nm, 1" dia
25	Fused Silica plano-convex lens, 75 mm f, 1" dia
26*	Right angle prism mirror, 15x15x15 mm

Abbreviations		
	R	Reflect
	T	Transmit
	f	Focal length
	CWL	Center wavelength
	FWHM	Full width half max (bandwidth)

*It is proposed to remove a beam splitter (#4, refer to Figure 2.2) and introduce a right angle prism mirror (#26) to reflect a fraction of 532-nm signal onto PMT active area to eliminate the vignetting occurring in the optical system due to the beam splitter mount.

Table 2.4. Transmission, reflection and efficiency for optics in each channel for LAPS detector.

List of optics/	**Channels (nm)**							
η	**660**	**607**	**528**	**530**	**532**	**295**	**283**	**277**
Telescope	R92	R92	R92	R92	R92	R92	R92	R92
Fiber (1)	T92	T92	T92	T92	T92	T90	T90	T90
Lens (2)	T93	T93	T93	T93	T93	T92	T92	T92
BS (3)	T93	T93	T93	T93	T93	R93	R93	R93
BS (4)*	T99	T99	T99	T99	R01	X	X	X
BS (7)	T94	R85	R96	R96	X	X	X	X
BS (8)	X	X	R60	T40	X	X	X	X
BS (13)	R96	T90	X	X	X	X	X	X
BS (18)	X	X	X	X	X	R98	T92	T94
BS (21)	X	X	X	X	X	X	R88	T75
OD (9a)	X	X	X	T25	X	X	X	X
Mirror(26)**	X	X	X	X	R92	X	X	X
BPF	T55	T55	T55	T55	T55	T12	T12	T12
Focus Lens	T92	T92	T92	T92	T92	T92	T92	T92
PMT QE	5	8	15	15	15	25	25	25
Total η (%)	1.7	2.2	3.1	0.5	0.05	1.9	1.6	1.4

where R## is the reflection efficiency in percentage,
T## is the transmission efficiency in percentage,
X for elements not in optical path for that channel.
All factors expressed as percentage to incident signal.

2.4 Receiving optics

A lidar receiver collects the return signal scattered from a laser-illuminated spot over a sequence of time bins corresponding to range of altitudes. A diagonal mirror transmits the laser beam along the receiver axis and creates a circular obscuration of 11-cm diameter for the receiving mirror. For the LAPS instrument, the return signal is collected by a 61-cm diameter parabolic mirror, which focuses the far field signal to an optical fiber positioned approximately 1.5 m (at focal length) from the mirror surface. The LAPS receiver system is simulated using ZEMAX, an optical systems modeling software, as shown in Figure 2.3.

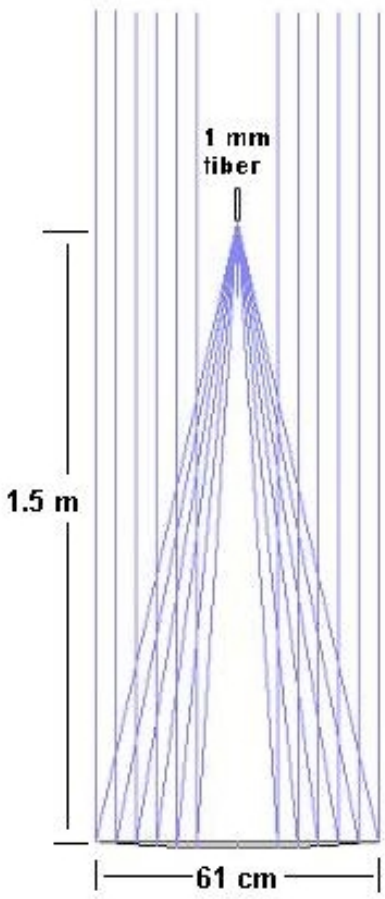

Figure 2.3. Simulation of LAPS receiver

An optical fiber facilitates efficient transfer of the optical signal to the detector box with its small 1-mm diameter serving as a field stop to limit the transfer of background light to the PMTs [Jenness et al., 1997]. For efficient capture of the convergent ray cone, the fiber's numerical aperture should be compatible with the receiver's *f* /D ratio [Jenness et al., 1997]. The LAPS instrument uses the Superguide G All–Silica SFS fiber from Fiberguide Industries. Specifications are shown in Table 2.5.

Table 2.5. Specifications of fiber used in LAPS instrument [Fiberguide, 2001]

	Core	Cladding
Material	SiO_2 (Suprasil)	Fluosil Standard
Refractive Index @ 633 nm	1.457	1.44

The Numerical Aperture (NA) of the fiber is 0.22 at 633nm as compared to the telescope, which has a NA of 0.2. The fiber NA remains within acceptable range for the several Raman wavelengths. The positioning of the fiber plays an important role in collection of return signals. If the fiber of diameter 1 mm is placed at infinity focus, it will capture the image of a far field spot since its diameter is greater than the blur circle of the far field spot. The blur circle image is caused by the divergence of the transmitted beam (0.1 mrad), which increases the angle of reflection of the rays from the telescope mirror surface (by 0.1 mrad). The diameter of the blur circle can be calculated as

$$\Delta d = 2f\Delta\theta \qquad [2.6]$$

where,

Δd is the diameter of the blur circle imaged at the fiber by the far field signal,

f is the focal length of the telescope = 1.5 m in case of the LAPS instrument,

$\Delta\theta$ is equal to the divergence of transmitted beam = 0.1 mrad.

For the LAPS receiver, the diameter of the blur circle is 0.3 mm when measured with the fiber positioned at infinity focus of telescope. However, if the fiber is positioned just beyond infinity focus, it can then capture rays converging from the near-field and all rays diverging from the far field [Jenness et al., 1997]. The improvement in collection efficiency with the fiber positioned just beyond infinity focus (optimally 1.7 mm beyond) is illustrated in Figure 2.4. The near-field rays that fall outside the diameter of the fiber can be collected by reflecting these rays by a mirror positioned at 45 degrees onto a secondary fiber, as shown in Figure 2.5.

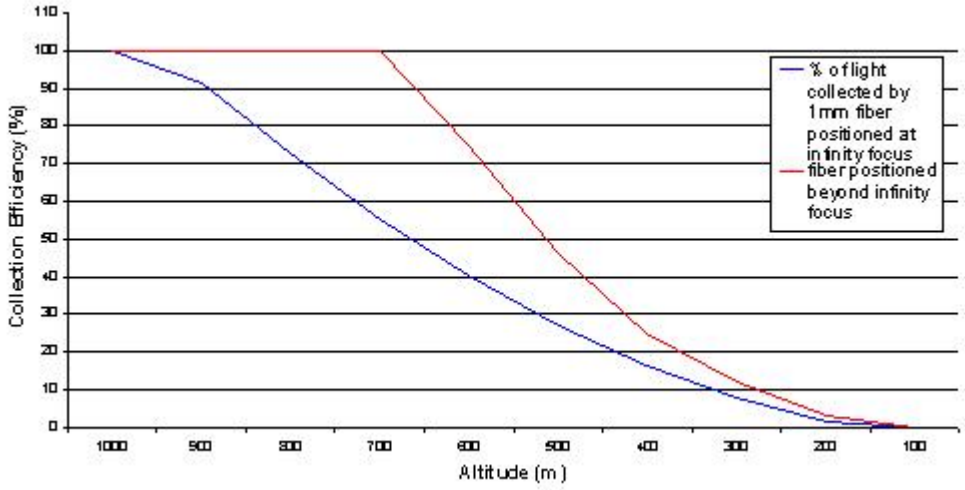

Figure 2.4. Variation in fiber collection efficiency with altitude for fiber positioned at infinity focus and just beyond it (optimum distance =1.7 mm beyond).

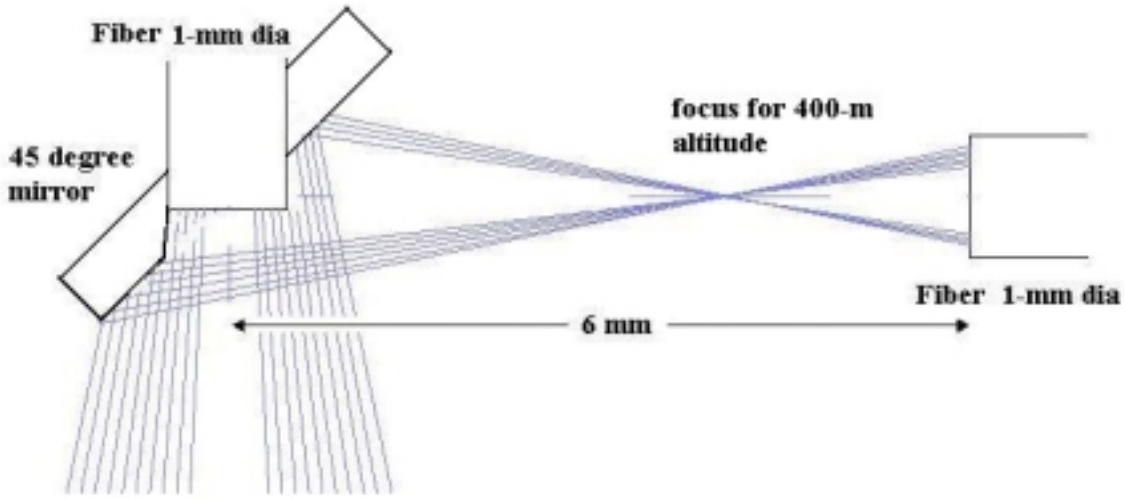

Figure 2.5. Receiver modification for capture of near-field rays using secondary fiber.

2.5 Limitations of LAPS detector

The LAPS instrument suffers from a number of inherent limitations. These are partly due to the unavailability of higher performance devices such as high speed PMTs at the time the instrument was built. Experience with operating the LAPS instrument over a number of campaigns has highlighted design and performance benefits to be gained from modifications to the original LAPS detector design. In the following sections we discuss several of these limitations and their adverse impact on measurements.

2.5.1 Vignetting

The return signals measured by LAPS instruments need to be corrected for losses due to the atmosphere, such as absorption, and due to the instrument, such as the telescope form factor. Another loss of signal that needed to be considered is the vignetting that occurs in the optics of the LAPS unit. Vignetting is the shadowing of rays

as they pass through an optical path [Hecht, 1990]. Due to this shadowing, signals from the near-field were being clipped, resulting in inaccurate data [Esposito, 1999]. Past data has shown that this vignetting occurs in both the visible and UV channels. The reasons for the vignetting to occur were due to clipping of the beam by positioning of an optical mount, improper focus onto the PMT active area, and misalignments in the system, etc. On reviewing the arrangement of the optics it was apparent that there was definite clipping in the visible channels due to a beam splitter mount, which was introduced into the LAPS detector in 1999 to detect the backscatter signal. For the UV channel, the cause of vignetting could be due either to misalignment or to improper focusing onto the PMT. Vignetting can result from the shift in the axis of beam transmission through a beam splitter caused by refraction. The rotational channels (528 nm, 530 nm) form the longest optical path in the system and thus diverge most over the distance of the path, thereby resulting in vignetting of the rotational channels. The vignetting occurring in the signals from altitudes below 800 m is shown in Figure 2.6. To test for vignetting during normal operation, the 528-nm filter was replaced by a 530-nm filter. The signal ratio during the vignetting run would remain constant over the full altitude range for a system free from vignetting. However the ratio in Figure 2.6 shows large variation in the near field. Assuming that transmission maintains the fiber modal characteristics of the collected signals, the near field signals would form near the periphery of the beam. The measurement suggests that the vignetting taking place in the system is due to clipping of the beam.

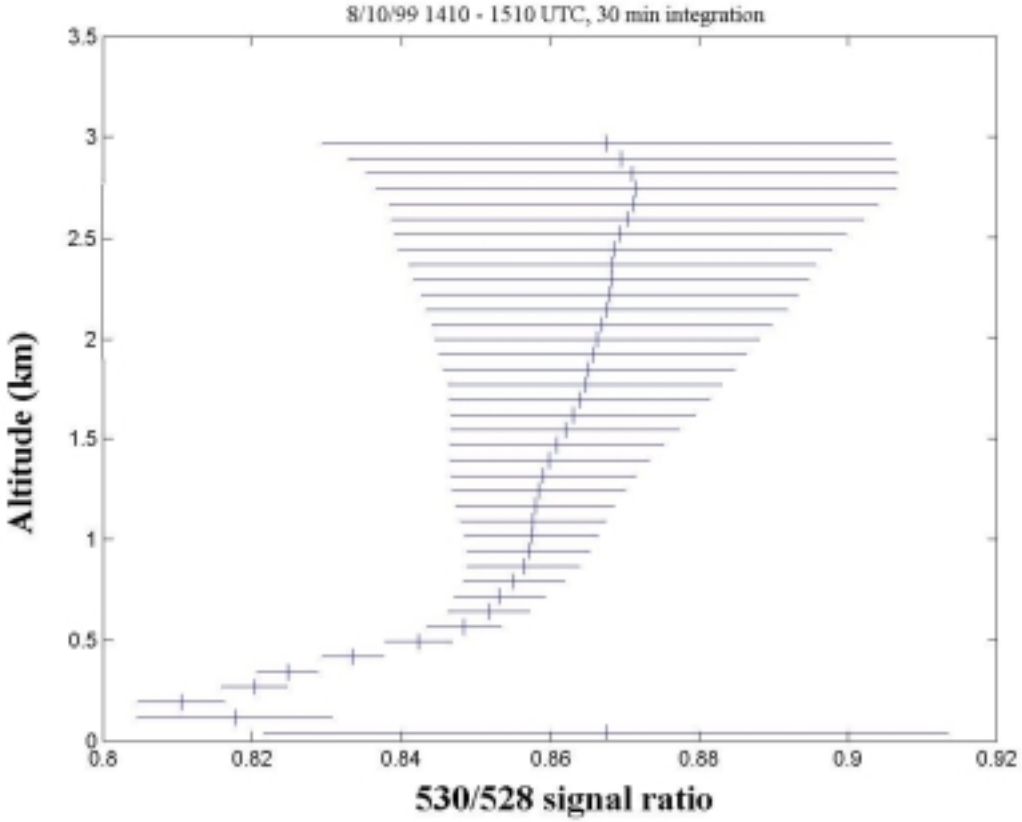

Figure 2.6. The signal ratio 530/528 with 530-nm filter in both channels.

2.5.2 Calibration scheme

The lidar calibration coefficient for water vapor measurements obtained with LAPS is determined by comparison with the mixing ratio derived from collocated, simultaneous radiosonde measurements of relative humidity and temperature. Even though the value is quite stable, this method presents a number of shortcomings if a long-term absolute calibration of lidar instruments is needed. The performance of radiosonde humidity sensors has been subject to a number of inter-comparison studies. Sonde-to-sonde variability due to differences in sensor materials and sensor calibration procedures, limits the precision in determination of the calibration coefficient [Philbrick et al., 1998a;

Sherlock et al., 1999a]. Also, the balloon sonde and lidar instrument sample the water vapor field quite differently in space and time. The lidar provides a time-averaged mixing ratio for an overhead column, whereas the radiosonde makes a set of point measurements along a path of horizontal wind drift of the balloon as it rises. Also since the radiosonde samples each altitude only once while ascending or descending, this can give rise to large measurement differences if the water vapor varies significantly over the sounding interval [Sherlock et al., 1999b]. The temperature dependence and the response characteristics of the radiosonde humidity sensor can also give rise to significant measurement differences. To ensure an independent measurement technique, the lidar instrument should be independently calibrated with a calibration procedure that accounts for variations in the optical characteristics of the components over time. An independent technique would also eliminate the need to have a simultaneous radiosonde or *in situ* radiometer measurement to monitor the lidar instrument performance.

2.5.3 Refraction through beam splitters

The LAPS detector uses a beam splitter arrangement to separate the Raman wavelengths. The beam splitters surfaces are coated to give the required wavelength separation on the front surface, and AR (anti-reflective) coating on their back surface, to illuminate the photocathodes of spatially separated PMTs. Light waves transmitting through a material undergo refraction, and in the case of the beam passing through the substrate of the splitter result in bending towards the normal of the surface, as shown in Figure 2.7.

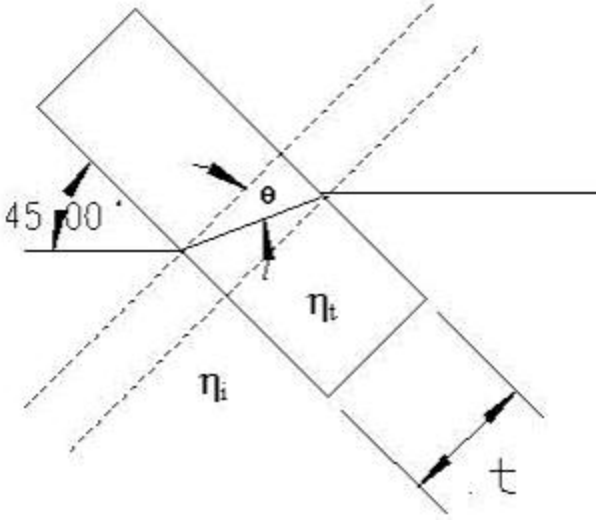

Figure 2.7. Shift in ray transmission observed due to refraction.

By the law of refraction,

$$\eta_i \sin\theta_i = \eta_t \sin\theta_t , \qquad [2.7]$$

This phenomenon has a significant bearing on the positioning of the active area of the PMT. If for instance, a beam that would be incident at the center of the PMT active area for a system that does not take refraction into account would be offset by Δx due to refraction through a beam splitter. Hence a design that assumes an axially symmetric light path would cause significant vignetting to occur in the detector unit, as shown in Figure 2.8.

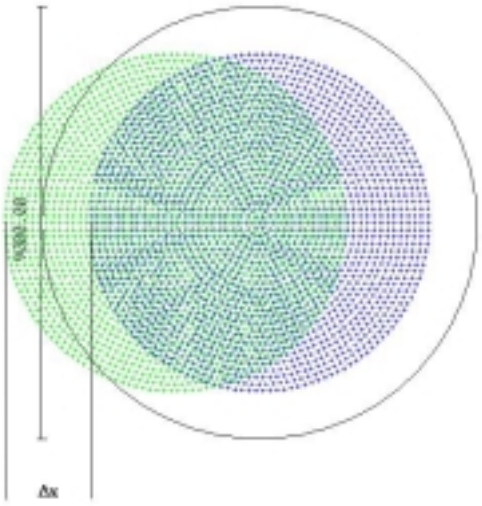

Figure 2.8. Shift in beam profile due to refraction at the PMT active area for an axially symmetric path for the 277-nm channel in the LAPS detector.

The effect of this shift is further amplified when we consider the design for the advanced detector system, where 5 parallel beam splitters reflecting the required Raman wavelength towards the PMT and transmitting the rest. This shift, Δx, can be computed for a given material of thickness t.

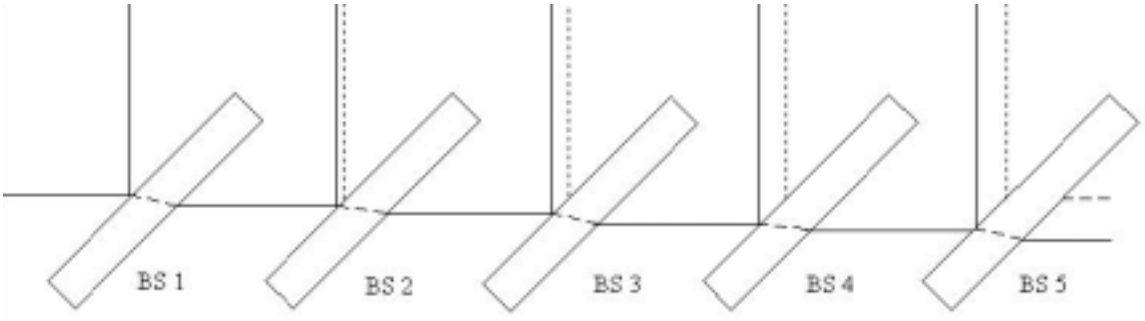

Figure 2.9. Shift due to refraction occurring when rays transmit through beam splitter.

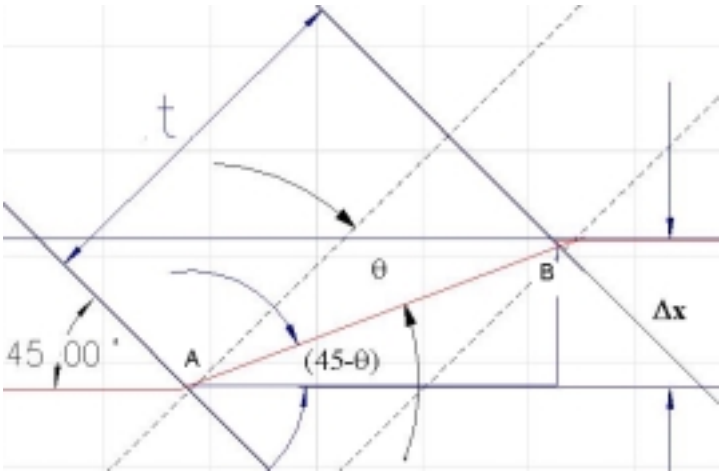

Figure 2.10. Mathematical calculation of beam shift in the LAPS/ advanced detector.

The shift through a single beam splitter of thickness t with refractive index of material η_t for 45^o incidence can be computed as,

$$\Delta x = (t /\cos [\sin^{-1}(1/ \sqrt{2}\eta_t)]).\sin (45 - \sin^{-1}(1/ \sqrt{2}\eta_t)). \qquad [2.8]$$

The shift due to each beam splitter can be calculated and added to the preceding beam splitter(s). The LAPS detector was aligned visually and compensation for this shift was made by adjusting the beam splitter angular position. For the advanced detector, this shift will be more significant and will prevent proper alignment due to more splitters contributing to the shift and the smaller photocathode areas. Adjusting the angular position of the beam splitters in the LAPS detector so that the shifted beam is focused at the center of PMT active area can compensate for most of this effect. However proper positioning of the beam splitters can account for the accumulated shift due to all the preceding beam splitters, and thus maintain the symmetric position and circular beam cross section at the photocathodes of each PMT.

2.5.4 Photomultiplier tubes

The most common photodetectors used in lidar systems at the visible and ultraviolet wavelengths are the photomultiplier tubes, or PMTs, which detect the signal strength. The PMT active area called a photocathode, emits an electron when a photon is incident on its surface, and the probability of occurrence is represented by a quantum efficiency, which is given as a fraction or a percent. Detector quantum efficiencies vary as a function of wavelength and typically have a maximum in the range from 0.1 to 0.3 for most PMTs of interest. The PMTs used in the LAPS detector are bulky and their large size is a limiting factor, which necessarily increases the optical path length. The PMT housing restricts the distance between adjacent channels to a minimum of 4 inches. In order to stabilize gain sensitivity, reduce dark current effects, and increase dynamic range, the PMTs in the LAPS detector are used in the photon counting mode. This means the individually generated current pulses for each photoelectron are counted rather than performing an A/D conversion on the DC current levels. The pulse width, determined by the rise and fall time, is crucial in determining the maximum count rate at which individual pulses can be discerned for the given PMT. The pulse width for the PMTs used in LAPS is typically about 2.5 ns giving a maximum count rate of about 400 MHz. The LAPS detector employs the Electron Tubes' models 9893B/350 (Bialkali) Q variant (quartz window) PMT for the ultraviolet channels and 9863B/350 (S20) for the visible channels, each with an effective cathode of diameter 9 mm. Efficiency curves for the above-mentioned models are shown in Figure 2.11.

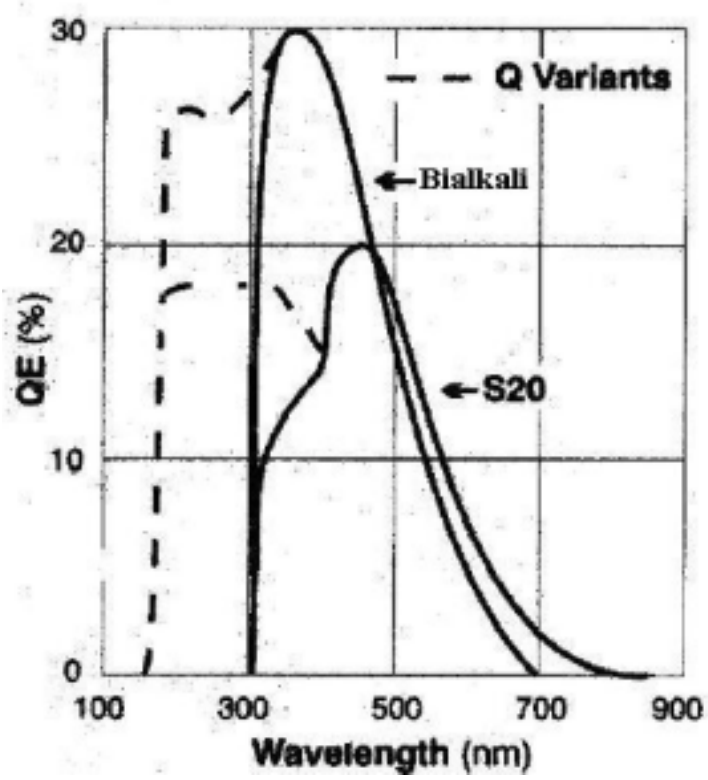

Figure 2.11. Quantum efficiency curves for the 9893 and 9863 series PMTs [Electron Tubes Inc., 2001]

2.6 LAPS optical design simulation

The optical path in the LAPS detector unit was simulated using optical simulation software called ZEMAX. The ZEMAX program can model, analyze and assist in the design of optical systems. The optical path in the detector unit basically consists of the multi-wavelength signal from a 1-mm diameter all silica fiber having a numerical aperture (NA) of 0.22 at 633 nm (see Table 2.5). This divergent beam is collimated using a plano-convex lens. The beam is separated into its component wavelengths by using dichroic beam splitters. The component wavelengths are then directed to their respective detectors through narrow band filters, which isolate the required wavelength. The fiber

output was simulated in ZEMAX using a point source diverged to represent the output divergence of the fiber. The lens used in the detector unit is a 38-mm focal length, 1-inch diameter UV fused-silica plano-convex lens. Using the simulated model we can determine the beam spot size, distance the lens should be placed from the fiber to obtain best results over the wide range of wavelengths, causes of vignetting and possibly a more optimal design for arrangement of PMTs. The optical path traversed by each wavelength has been analyzed and the beam spot size for each wavelength determined. No optimization is performed on this simulation, as the intent is to model the current optical design and understand the improvements that could be made. Figure 2.12 shows the simulation performed for the 528-nm channel, which has a total optical path length of about 450 mm. Figure 2.13 shows the 660-nm channel, which has a total optical path of 310 mm. Simulations were also performed for the UV channels. The optical simulation shown in Figure 2.14 is for the 277-nm channel, which has a total path length of 280 mm. The beam splitters in the LAPS detector, mounted at 45 degrees to the incidence radiation, are simulated by using a function called co-ordinate break in ZEMAX. This alters the path of the rays by the specified angle, 90 degrees in this case.

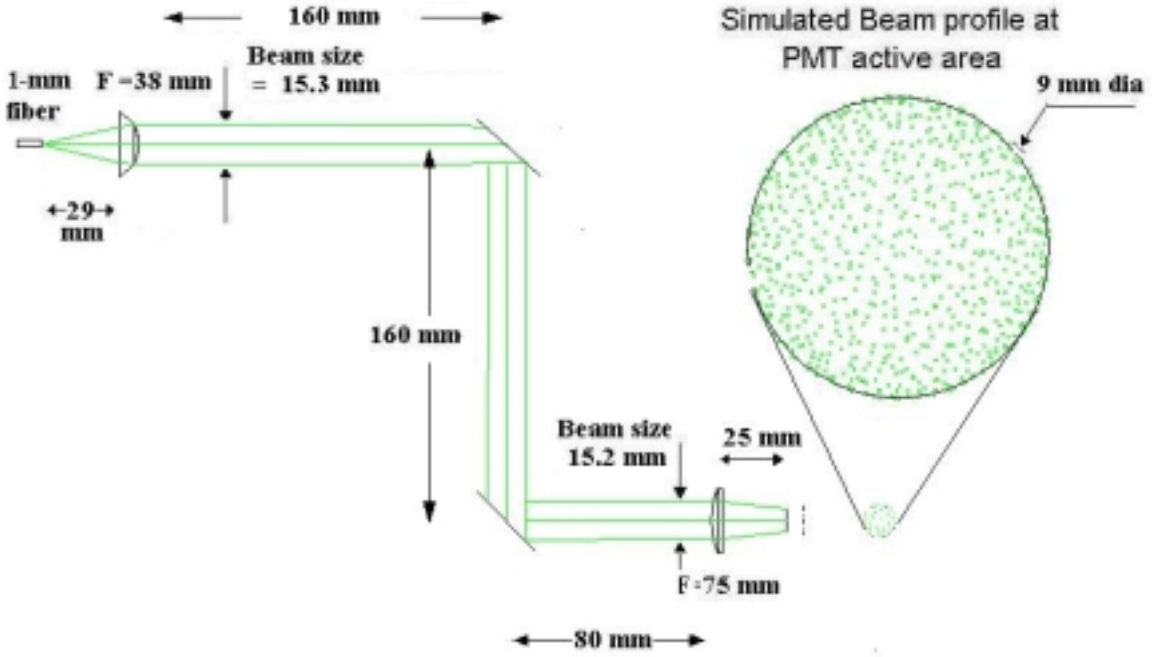

Figure 2.12. Optical path simulation for 528-nm channel in current LAPS detector design.

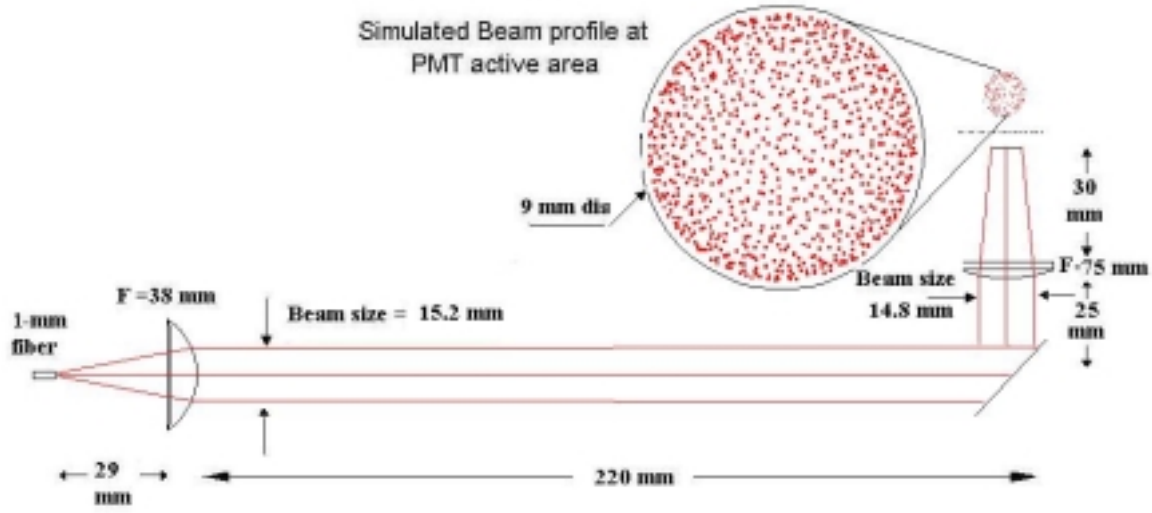

Figure 2.13. Optical path simulation for 660-nm channel in current LAPS detector design.

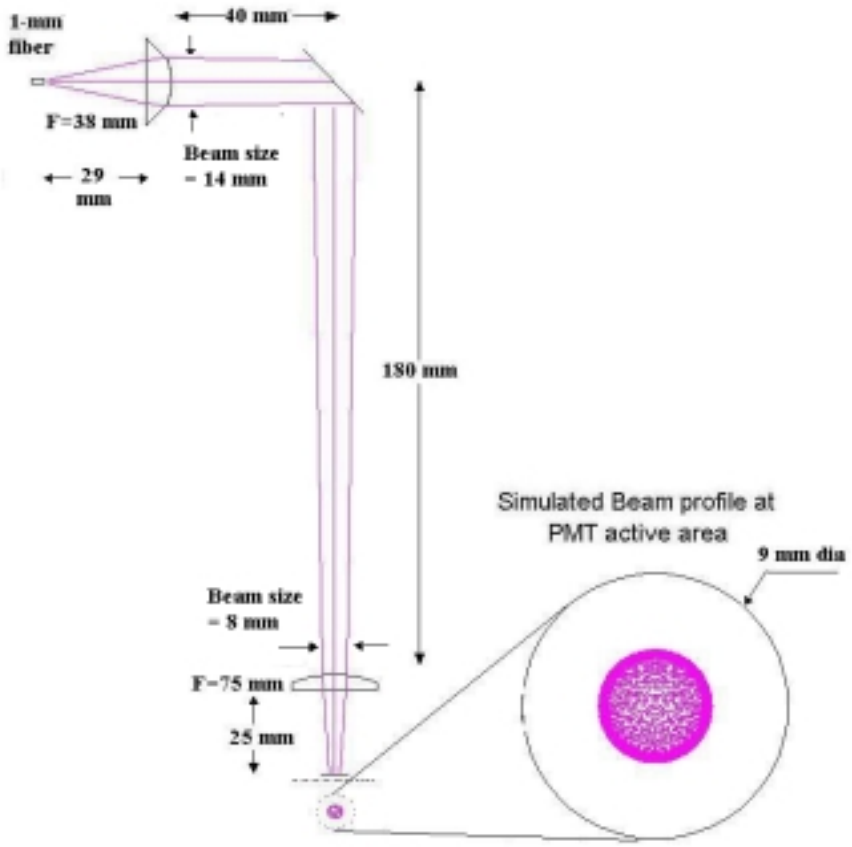

Figure 2.14. Optical path simulation for 277-nm channel in current LAPS detector design.

Simulation of the current detector using ZEMAX has highlighted the improvements that need to be made to the current optical design. A 75-mm focal length plano-convex lens positioned after the filter focuses the beam onto the PMT active area, of diameter 9 mm. The beam spot size can be made smaller by using a shorter focal length lens and also a more optimal design could yield shorter path lengths, ensuring that the divergence over distance is kept as small as possible. The angular incidence of the ray path can affect the bandwidth and center wavelength of the filters. These design issues and their ramifications will be discussed in more detail in the later sections. Experimental tests were performed to verify the simulation results. The beam size and intensity

distribution of the collimated beam were measured along the optical path and are shown in Figure 2.15. The experimental results (beam size=15 mm) were found to be in close agreement with simulated results (beam size=15.3 mm). Measurements were also made at the PMT active area, and were again found to agree with the simulated results. The beam size observed in the green channels was much bigger than the active area of PMT and would explain the vignetting occurring in the temperature measurements. This can be corrected by using a shorter focal length lens (f 25 mm) for collimating the fiber output. This would result in smaller beam sizes, which was verified experimentally, as shown in Figure 2.16. The experimental results (beam size=10.5 mm) were found to be in close agreement with simulated results (beam size= 10.3 mm), using a plano-convex lens of focal length 25 mm for collimation.

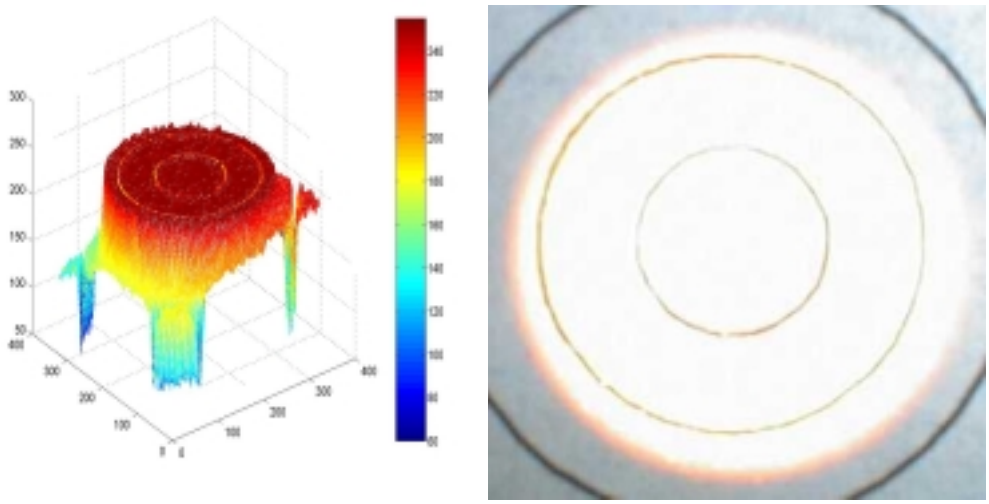

Figure 2.15. Intensity distribution and beam size using plano-convex lens with focal length 50 mm, measured 50 mm behind lens.

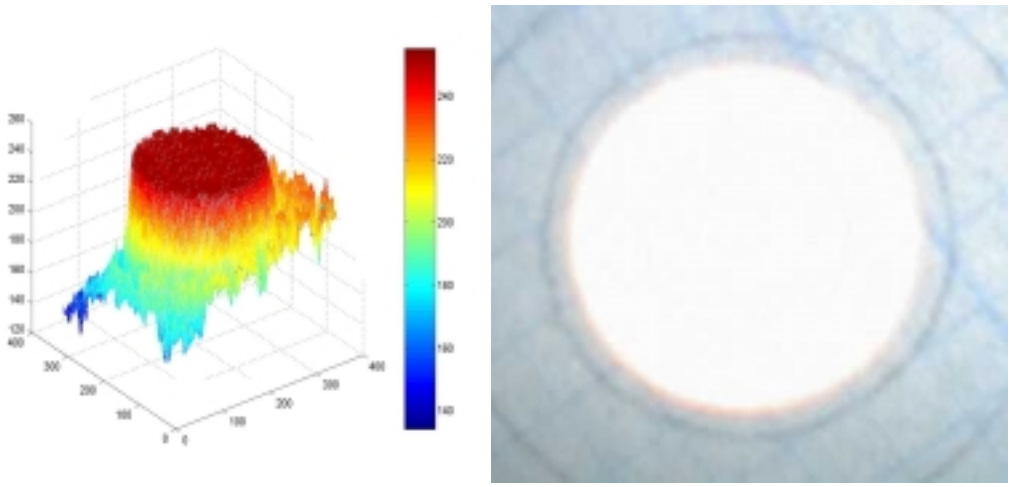

Figure 2.16. Intensity distribution and beam size using plano-convex lens with focal length 25 mm, measured 50 mm behind lens.

Chapter 3

Advanced Detector Design

3.1 Introduction

The LAPS instrument was used extensively in campaigns over a number of years and provided a valuable source of data for atmospheric studies. However, as the LAPS unit moves closer to being developed as a commercial product, there are significant improvements that could be made to reduce the extent of data processing and analysis corrections required. There are also design changes that could bring about substantial cost reduction and improvement in performance. As explained in Chapter 2, the LAPS detector system had several inherent limitations, which affected the quality of data collected. The advanced detector design aims to eliminate these uncertainties in measurements and also be more commercially viable than its predecessor. Measurements obtained from the LAPS instrument have been calibrated against other collocated sources. For these measurements to be made independently, the design needs to incorporate some type of self-calibration scheme for measurements of atmospheric constituents.

The primary purpose of the detector unit is to steer the Raman wavelengths to their respective PMTs. The spectral and spatial separation of the signals can be achieved in a number of ways. The collimated fiber output could be made incident on reflection gratings designed to spatially separate wavelength bands. The Raman wavelengths can be isolated using very narrow band-pass filters. This method would significantly reduce the background noise accompanying the signal. However, reflection gratings offer low levels

of efficiency over the wavelengths used and hence would result in lower SNR levels. The second method involves using optical fibers within the detector unit. However, this method still requires some form of wavelength separation using beam splitters. For the advanced detector, we propose to continue the use of an open optical system using beam splitters for wavelength separation. The optical element layout is shown (see Figure 3.1).

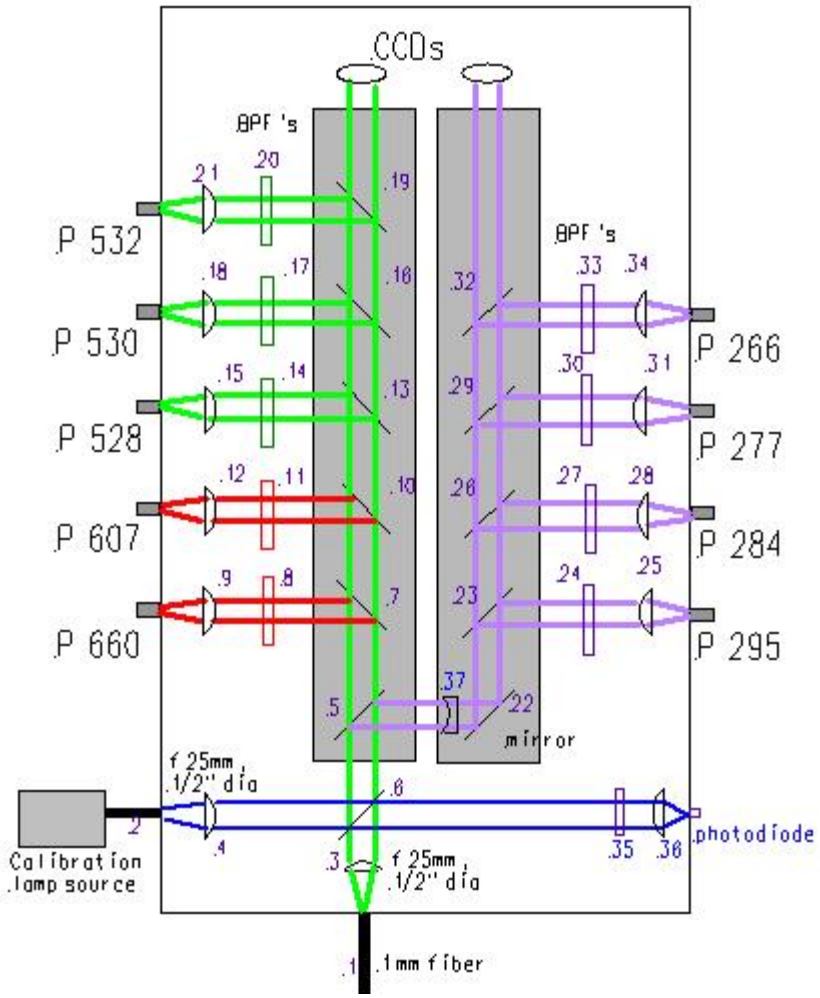

Figure 3.1. Optical element layout for advanced detector design.

The advanced design would incorporate a self-calibration mechanism using a filter-switching slide, which would be used to determine the relative transmission and

efficiency of the channels. Table 3.1 lists the optical elements used in the detector with the reference number as referred to Figure 3.1.

Table 3.1. List of optical components for advanced detector design (see Figure 3.1).

Ref. #	Description
1	Superguide G All–Silica SFS fiber, NA=0.22,1-mm dia core
2	Superguide G All–Silica SFS fiber, NA=0.22,1-mm dia core
3	Fused Silica plano-convex lens, 25 mm f, 12.7 mm dia, wideband AR coated.
4	Fused Silica plano-convex lens, 25 mm f, 12.7 mm dia, wideband AR coated.
5	Beamsplitter R: 266, 277, 283, 294 nm T: 532, 528, 530, 607, 660 nm
6	Mirror, UV enhanced aluminum, 1” dia
7	Beamsplitter R: 660 nm T: 532, 528, 530, 607 nm
8	Metal Oxide narrow band filter, CWL=660.35 nm FWHM=0.15 nm,1” dia
9	BK7 plano-convex lens, 50 mm f, 1” dia
10	Beamsplitter R: 607 nm T: 532, 528, 530 nm
11	Metal Oxide narrow band filter, CWL=607.37 nm FWHM=0.15 nm,1” dia
12	BK7 plano-convex lens, 50 mm f, 1” dia
13	Beamsplitter R:30% T:70%, wideband
14	Metal Oxide narrow band filter, CWL=528 nm FWHM=0.15 nm,1” dia
15	BK7 plano-convex lens, 75 mm f, 1” dia
16	Beamsplitter R:90% T:10%, wideband
17	Metal Oxide narrow band filter, CWL=530 nm FWHM=0.15 nm,1” dia
18	BK7 plano-convex lens, 75 mm f, 1” dia
19	Beamsplitter R:50% T:50%, wideband
20	Metal Oxide narrow band filter, CWL=532 nm FWHM=0.15 nm,1” dia
21	BK7 plano-convex lens, 75 mm f, 1” dia
22	Mirror, UV enhanced aluminum, 1” dia
23	Beamsplitter R:294 nm T:266, 283, 277 nm
24	Metal Oxide narrow band filter, CWL=294.65 nm FWHM=0.25 nm,1” dia

25	Fused Silica plano-convex lens, 100 mm f, 1” dia
26	Beamsplitter R:283 nm T:266, 277 nm
27	Metal Oxide narrow band filter, CWL=283.61 nm FWHM=0.25 nm,1” dia
28	Fused Silica plano-convex lens, 100 mm f, 1” dia
29	Beamsplitter R:277 nm T:266 nm
30	Metal Oxide narrow band filter, CWL=277.51 nm FWHM=0.25 nm, 1” dia
31	Fused Silica plano-convex lens, 100 mm f, 1” dia
32	Beamsplitter R: 50% T:50%
33	Metal Oxide narrow band filter, CWL=266.025 nm FWHM=0.25 nm, 1” dia
34	Fused Silica plano-convex lens, 100 mm f, 1” dia
35	Filter wheel, containing filters: 8, 11,17,24,27,30
36	Fused Silica plano-convex lens, 75 mm f, 1” dia
37	Fused Silica plano-concave lens, -200 mm f, 1” dia

Abbreviations

R	Reflect
T	Transmit
f	Focal length
CWL	Center wavelength
FWHM	Full width half max (bandwidth)

Table 3.2 lists the transmission, reflection and efficiency factors of the optical elements in each channel. The total optical efficiency for each channel is computed by multiplying these factors for each channel. The total efficiency is expressed as a percentage of the total number of photons counted by the photomultiplier tube to the total number of photons incident on the mirror surface for that wavelength. The total efficiency computed in Table 3.2 would be valid for altitudes above 800 m. Below 800 m the efficiency varies as a function of the telescope form factor.

Table 3.2. Transmission, reflection and efficiency for optics in each channel for advanced detector design.

List of optics/ η	Channels (nm)								
	660	**607**	**528**	**530**	**532**	**295**	**283**	**277**	**266**
Telescope	R92	R92	R92	R92	R92	R92	R92	R92	R92
Fiber (1)	T92	T92	T92	T92	T92	T90	T90	T90	T90
Lens (3)	T93	T93	T93	T93	T93	T92	T92	T92	T92
BS (5)	T93	T93	T93	T93	T93	R93	R93	R93	R93
BS (7)	R97	T92	T92	T92	T92	X	X	X	X
BS (10)	X	R97	T92	T92	T92	X	X	X	X
BS (13)	X	X	R70	T30	T30	X	X	X	X
BS (16)	X	X	X	R90	T10	X	X	X	X
BS (19)	X	X	X	X	R50	X	X	X	X
Mirror (22)	X	X	X	X	X	R92	R92	R92	R92
BS (23)	X	X	X	X	X	R98	T94	T94	T94
BS (26)	X	X	X	X	X	X	R90	T80	T80
BS (29)	X	X	X	X	X	X	X	R90	T80
BS (32)	X	X	X	X	X	X	X	X	R50
BPF	T55	T55	T55	T55	T55	T20	T20	T20	T20
Focus Lens	T90	T90	T90	T90	T90	T92	T92	T92	T92
PMT QE	11	11	15	15	15	30	30	30	30
Total η(%)	4.1	3.8	2.6	1.0	0.5	3.5	3.0	2.4	0.5

Where R## is the reflection efficiency in percentage,
T## is the transmission efficiency in percentage,
X for elements not in optical path for that channel.
All factors expressed as percentage to incident signal.
Number in bracket following optics element refers to elements labeled in Figure 3.1

3.2 Optical Simulation

Light collected by the telescope mirror is focused into a 1-mm fiber, which transfers the signal to the detector unit. Light output from the fiber diverges at an angle equal to the arcsine of NA of the fiber. This light is collimated using a 25-mm focal length, 12.7-mm diameter fused-silica plano-convex lens. This lens has a shorter focal length than the one employed in the LAPS detector and results in a smaller beam spot size. Optical simulations were performed for each of the Raman wavelengths to

determine the beam size and collimation. The advanced detector uses an arrangement of beam splitters to separate the wavelengths. The Raman wavelengths are then isolated using a very narrow band-pass filter having a bandwidth of 0.15 nm for visible and 0.25 nm for UV wavelengths. The output beam from the filter is then focused by a plano convex lens onto the active area of the PMT. The simulation shows that the ultraviolet wavelengths tend to converge at a distance after being collimated by the initial plano-convex lens. Transmission through a filter depends on the angle of incidence and a converging beam would result in shifting the center wavelength of the filter and broadening the band pass. The 660-nm beam size was determined to be about 10.3 mm as shown in Figure 3.2. It was then focused to illuminate a circular area of diameter 6 mm on the PMT active area of 8-mm diameter. The beam spot image generated by multiple rays onto the PMT active area is shown within a circular area of diameter 6 mm along with the ray trace diagram. Figures 3.3 and 3.4 give similar information about the 530-nm and 295-nm wavelength. Focal length of a lens varies as a function of wavelengths (see Appendix). The UV rays, which would have a shorter focal length for the lens used, tend to converge at a distance of 248 mm after the lens surface. An off-normal incidence would shift the center wavelength of the filter and also increase the bandwidth. A plano-concave lens of focal length –200 mm placed in the UV path would reduce the divergence. Similar simulations were performed for the other channels (see Appendix).

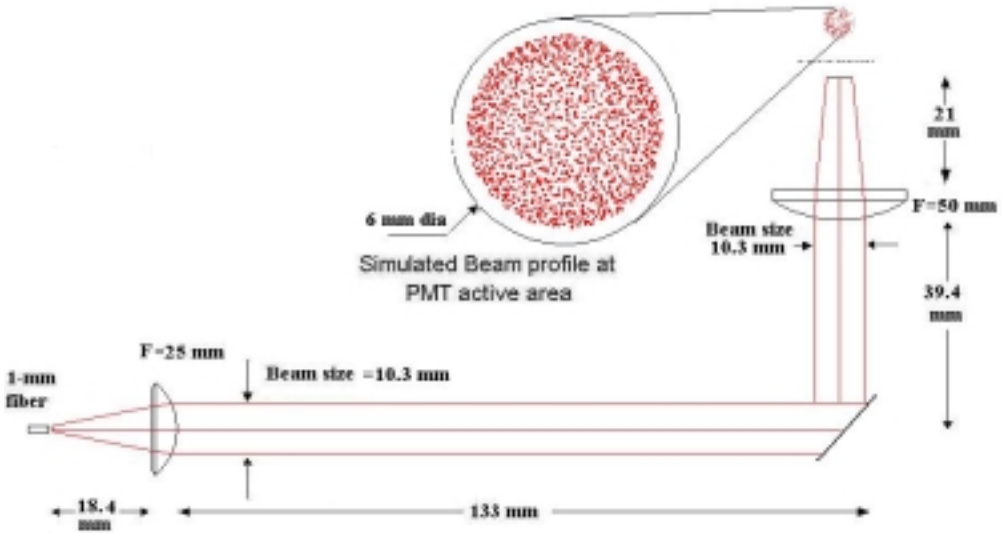

Figure 3.2. Optical path simulation and beam size of 660-nm channel in advanced detector system.

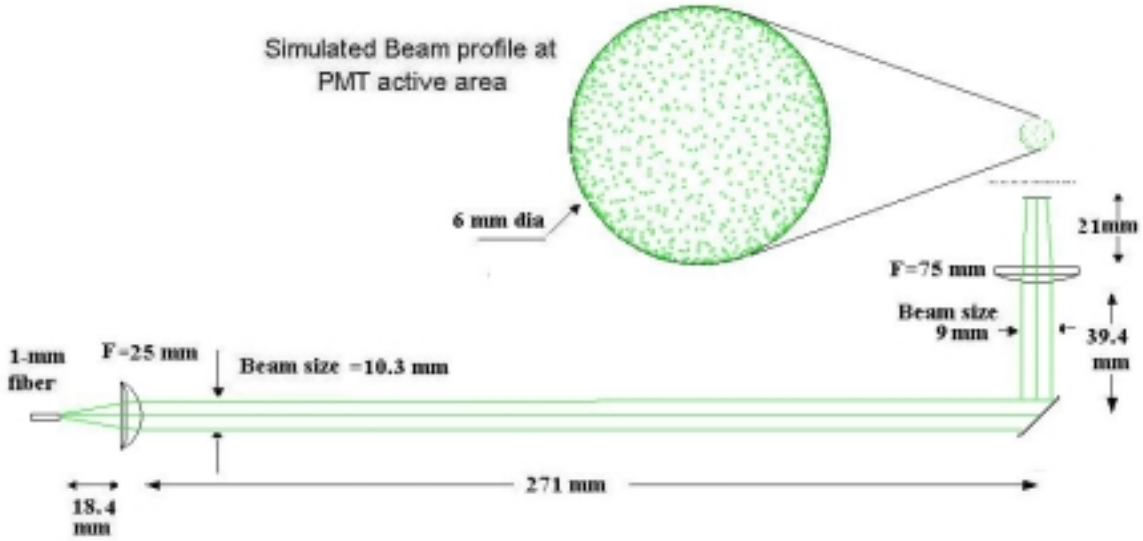

Figure 3.3. Optical path simulation and beam size of 530-nm channel in advanced detector system.

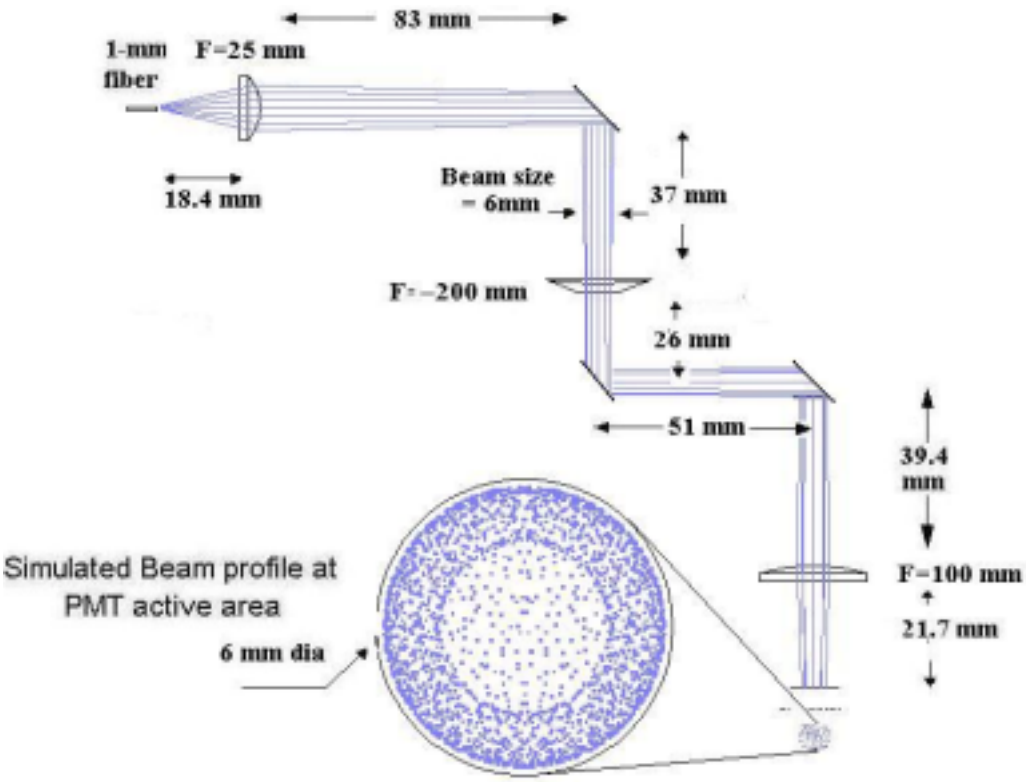

Figure 3.4. Optical path simulation and beam size of 295-nm channel in advanced detector system.

3.3 Mechanical design

A major objective when designing the advanced detector unit was to eliminate the problems found in the LAPS detector. The advanced detector employs a filter selection slide mechanism to allow for self-calibration of the unit. This is achieved by housing the filters for a specific channel in an aluminum block, with the vertical movement of the block controlled via the terminal. The beam splitters are housed in a solid aluminum block in slots machined at an angle of 45 degrees. They are held in position using nylon head set screws. This method of housing the beam splitter elements will reduce problems due to misalignments found in the LAPS detector, will reduce stray light, and will be more economical to implement for a commercial instrument. The positioning of the beam

splitters along the path is constrained by the size of the PMT housing and adjusted for transmission shift of the beam through the beam splitter. Each PMT is housed in an aluminum box and mounted on an aluminum sheet, which in turn is screwed onto the detector wall. The PMT housings are mounted with their centers separated by a distance of 2 inches. The beam splitters are positioned at a distance of 2 inches + total Δx (calculated from Equation 2.7 for each beam splitter and accumulated for the preceding beam splitters). The first beam splitter in the detector transmits the visible and reflects the UV wavelengths and is positioned normal to the rest of the beam splitters in the visible beam splitter housing. It will shift the beam in the direction opposite to the rest of the beam splitters in the visible path and is denoted as $-\Delta x$ for simplicity in calculation. The beam splitters causing the shift in the UV channels are all parallel to the first beam splitter that reflects the UV wavelengths. A deuterium lamp is used to illuminate the photocathodes for calibration purposes and lamp output is coupled to the detector using a fiber. The beam from the fiber is directed along the data signal path using a mirror mounted at 45 degrees on a slide, which provides a shutter for the data signal and passes the calibration signal. The slide has an open position during normal operation to allow the signal beam to pass through. Figure 3.5 shows the top view of the detector box.

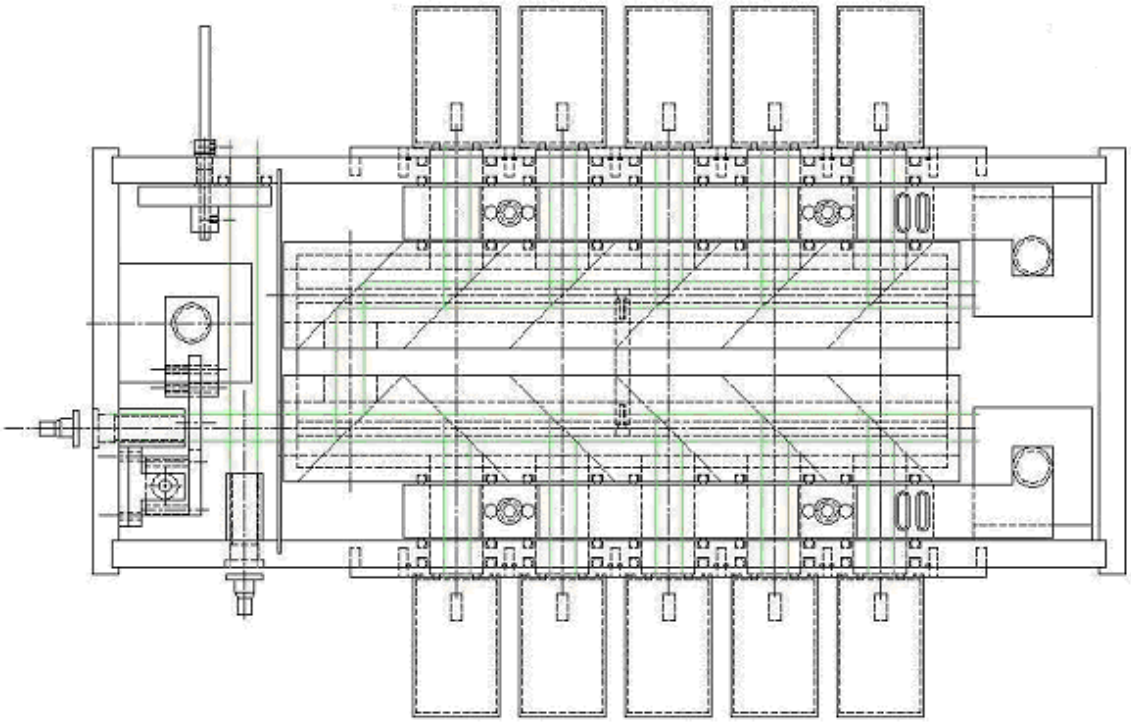

Figure 3.5. Mechanical drawing showing the top view of advanced detector box (prepared by Alex Achey)

Chapter 4

Improvements in Detector Design

4.1 Self calibration scheme

Conventional lidar instruments employ the following techniques for calibration: (1) comparison with simultaneous collocated vertical profile measurement such as a radiosonde, or (2) comparison at a single altitude using a fixed-height *in situ* sensor. The calibration factor describes the instrument transmitter, receiver and detection efficiency for the signals at the Raman wavelengths. To ensure an independent measurement technique, the lidar instrument must be independently calibrated with a calibration procedure which accounts for variations in the optical characteristics of the components over time. Relative transmission and efficiency factors based purely on manufacturer's data would introduce errors in the calibration factor, as these characteristics are susceptible to variations with environmental conditions and time. For the detector design in the ALAPS instrument we propose a self-calibration scheme based on frequent, perhaps daily, experimental determinations of the ratios of the transmission and efficiency factors. The total transmission is given by the product of the transmissions of the individual optical components including the filters used to select the Raman return signals, beam splitters, collimating lenses; the reflection coefficients of the telescope, beam splitters and mirrors; and the quantum efficiency and gain factors of the PMTs, for each wavelength. A practical calibration approach is to reduce the question of the instrument sensitivity for each of the Raman measurements to a simple ratio of the

Raman cross sections. Thus calibration can be accomplished because the Raman measurements use the ratios of signals. By interchanging the filters in the beam paths, it is possible to directly determine the calibration constant using the Raman scattering cross-sections which are known to high accuracy.

4.1.1 Filter switching

The lidar detector employs narrow-band filters to isolate the Raman wavelengths from background light and the other wavelengths. A filter slide arrangement would permit a computer-controlled calibration sequence of filter selection in each channel. Identical filters prepared by the manufacturer in the same batch would be used in each channel for the ratio measurement.

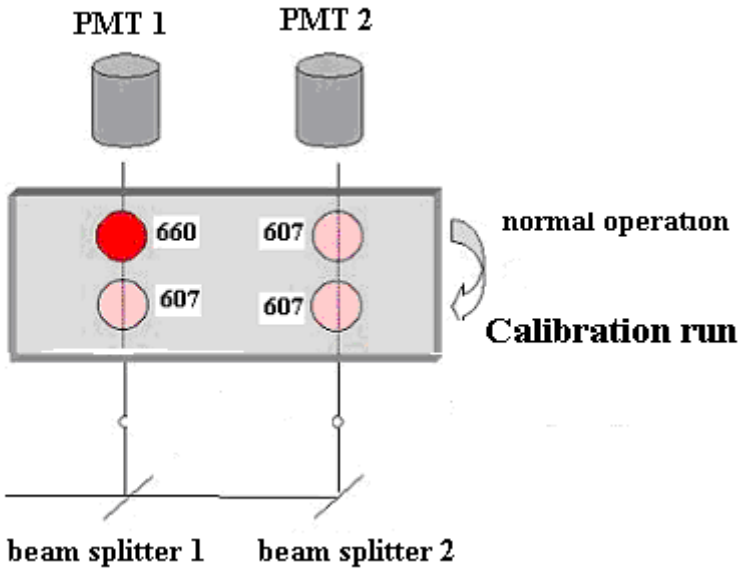

Figure 4.1. Self-calibration scheme illustrated for water vapor measurements.

The net optical efficiency $\xi_R(\lambda_R)$ in the lidar equation (see Equation 2.1) can be determined by the product of the transmission, reflection and efficiency factors for the individual elements:

$$\xi_R(\lambda) = R_{telescope}(\lambda) * \text{ Telescope form factor}(\lambda) * T_{fiber}(\lambda) * T_{lens}(\lambda) * T_{beam\ splitter(s)}(\lambda) * R_{beam\ splitter(s)}(\lambda) * T_{filter}(\lambda) * QE_{pmt}(\lambda) \quad [4.1]$$

$R_{telescope}(\lambda_1) = R_{telescope}(\lambda_2)$, as this factor is constant over the λ in consideration. [4.2]

Telescope form factor(λ_1) = Telescope form factor(λ_2) for same altitude [4.3]

$T_{fiber}(\lambda_1) = T_{fiber}(\lambda_2)$, fiber efficiency is assumed constant over λ in consideration. [4.4]

$$\frac{\xi_R(\lambda_1)}{\xi_R(\lambda_2)} = \frac{T_{lens}(\lambda_1) * T_{beam\ splitter(s)}(\lambda_1) * R_{beam\ splitter(s)}(\lambda_1) * T_{filter}(\lambda_1) * QE_{pmt}(\lambda_1)}{T_{lens}(\lambda_2) * T_{beam\ splitter(s)}(\lambda_2) * R_{beam\ splitter(s)}(\lambda_2) * T_{filter}(\lambda_2) * QE_{pmt}(\lambda_2)} \quad [4.5]$$

The calibration scheme is illustrated in Figure 4.1 and is derived mathematically for water vapor measurements. Water vapor mixing ratio, also known as specific humidity, is measured at both ultraviolet and visible wavelengths. The water vapor mixing ratio is determined by taking the ratio of the Raman signal for water vapor to the signal for molecular nitrogen, which represents a constant value of 78% of the atmosphere. The water vapor mixing ratio is calculated by taking the ratio of the return signal at two different wavelengths, i.e., the 1st Stokes vibrational Raman-shifted wavelengths of water over nitrogen, and multiplying by a calibration factor. The return signal of nitrogen (607 nm for visible channels, 284 nm for ultraviolet channels) is used to determine the density of ambient air. The following equation is used to determine the vertical profiles of water vapor, W(z) [Esposito, 1999],

$$W(z) = K_{cal}\frac{S_{H2O}(z)}{S_{N2}(z)}, \quad [4.6]$$

where,

S_{H2O} is the received signal from the vibrational Raman shift of H_2O at 660,

S_{N2} is the received signal from the vibrational Raman shift of N_2 at 607,

K_{cal} is a calibration constant given by

$$K_{cal} = K_{opt} \cdot \frac{\sigma_{H2O}}{\sigma_{N2}} \qquad [4.7]$$

where

$$K_{opt} = \frac{\text{Optical efficiency (660 nm detector channel)}}{\text{Optical efficiency (607 nm detector channel)}}$$

The calibration sequence would be programmed to execute at predetermined intervals. The filter selection slide would be moved to position nitrogen filters in the optical path of both channels. The beam splitter transmission and reflection characteristics allow sufficient signal to be incident on the PMT active area at each wavelength. With narrow band nitrogen filters in both channels, the PMTs in each channel would detect the signal at 607 nm. The photon count ratio (N_{660} / N_{607}) gives the relative transmission of the optical components for the two channels. The calibration scheme requires precise determination of the transmission coefficients for each filter using a spectrophotometer. The ratios of the Raman scattering cross sections for water vapor and nitrogen are known accurately [Measures, 1984]. With the slide positioned for normal operation, i.e., 660-nm filter in water vapor channel and 607-nm filter in nitrogen channel, the water vapor mixing ratio is derived.

$$\text{Water vapor mixing ratio} = \frac{T_R D_1 S_1 T_{660} \sigma_{H2O} N_{660}}{T_R D_2 S_2 T_{607} \sigma_{N2} N_{607}} \quad [4.8]$$

where,

T_R is the transmission efficiency of the optical components common to the two channels,

D_1, D_2 are the PMT quantum efficiencies for the water vapor and nitrogen channel (channel 1, 2) respectively,

S_1, S_2 are the beam splitter transmission/reflection factors for the water vapor and nitrogen channel respectively,

T_{660}, T_{607} are the filter transmissions for 660-nm and 607-nm wavelengths respectively,

σ_x is the is the Raman cross-section of species x at the laser wavelength,

Calibration run

With narrow band nitrogen filters in both channels,

$$\frac{T_R D_1 S_1 T_{607} \sigma_{N2} PC_1}{T_R D_2 S_2 T_{607} \sigma_{N2} PC_2} = 1 \quad [4.9]$$

where,

PC_1 and PC_2 are the number of photons counted by channel 1and 2 respectively.

From Equation [4.9],

$$\frac{PC_1}{PC_2} = \frac{D_2 S_2}{D_1 S_1} \quad [4.10]$$

$$K_{opt} = \frac{PC_1 T_{660}}{PC_2 T_{607}} \quad [4.11]$$

$$K_{cal} = K_{opt} * \frac{\sigma_{H2O}}{\sigma_{N2}} \quad [4.12]$$

$$\frac{\sigma_{H2O}}{\sigma_{N2}} = 39/14 \quad \text{[Measures, 1984]}$$

Normal Run

N_{660} = Photons counted by PMT in the H_2O channel

N_{607} = Photons counted by PMT in the N_2 channel

$$\text{Water vapor mixing ratio} = K_{cal} \frac{N_{660}}{N_{607}} \quad [4.13]$$

Hence the water vapor mixing ratio can be determined from the signal ratios, using the self-calibration scheme incorporated in the advanced design. Similar scheme is incorporated to determine the relative transmission factors for each of the other Raman ratio measurements also.

4.1.2 External light source

Complementary to the filter-slide calibration scheme, we also propose to monitor the instrument transmission and detection efficiency at the Raman wavelengths by using an external light source with a continuous spectrum. This scheme would incorporate a UV-VIS light source having a stable and predictable spectrum over the wavelengths under consideration. The output would be made incident to the detection system to replicate the path and beam size of the signal beam, details of which are illustrated in the mechanical design for the advanced detector. By illuminating the detection system with a

light source whose spectrum is known or can be modeled, the relative transmission factors for the channels can be evaluated. After evaluating a number of light sources, the deuterium lamp was chosen for calibration purposes. Deuterium lamps have continuous spectra from UV-VIS with relatively high power in the UV, which falls off significantly in the visible. A blocking filter with high absorption in the UV and relatively lower absorption in the visible will be used in conjunction with the lamp to obtain a flat transmission spectrum. To ensure that we remain in the linear region of the photon counters, neutral-density filters will be placed in the beam path before the dichroic mirror. The low-pressure source lamp is powered by a highly stable supply. It is enclosed in a protective housing and has a fiber coupler to feed the light into the detector box.

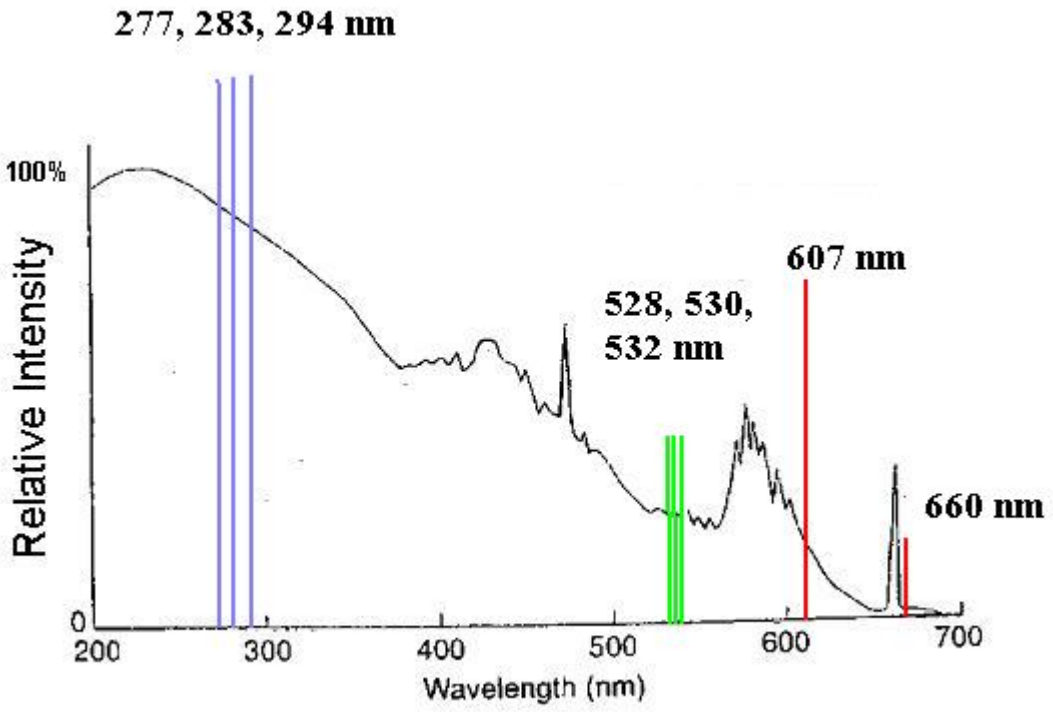

Figure 4.2. Relative intensity spectral data for deuterium lamp [Cathodeon, 2001]

The relative intensity at the Raman wavelengths is determined using a filter wheel arrangement, which would position the appropriate narrow band-pass filter in the beam path. A plano-convex lens, f 75 mm, focuses the light onto the active area of a silicon photodiode and the relative intensity for wavelengths can be determined accurately. In the calibration mode, the slide is positioned to allow the beam from the calibration lamp to be deflected into the optical system. Ratio of the photon count for two channels (e.g., 660 nm and 607 nm) should be equal to the relative intensity for a system that transmits and detects equally for both wavelengths. The ratio for the advanced detector design would be altered due to variations in beam splitter ratios, filter transmission factors, QE of the PMT, etc. The relative intensity measured by the photodiode combined with the scattering cross sections at the wavelengths will provide a second calibration constant for the measurement. Results from the two approaches will be compared and used for the ALAPS detector design.

4.2 Narrow band filters

The advanced detector employs very narrow band-pass filters for the Raman wavelength isolation. The Raman-shifted wavelengths for excitation with a 532-nm and 266-nm pulse can be calculated (see Table 4.2) using the Raman-shifted wave-number from Table 4.1. Narrow band-pass filters designed for these center wavelengths allow isolation of the Raman lines and increase the signal to noise ratio by rejecting the out-of-band wavelengths.

Table 4.1.Raman wave-number shifts [Measures, 1984].

Molecule	Raman shift (cm^{-1})
N_2	2330.7
H_2O	3651.7
O_2	1556

Shifted Wave number=wave number of desired λ -Raman shift (see Table 4.1) [4.14]

Shifted λ =1/shiftedWavenumber [4.15]

The Raman-shifted wavelength for transmitted laser wavelengths is calculated in Table 4.2.

Table 4.2. Raman shifted wavelengths for given excitation.

Excitation λ →	**266.025 nm**	**354.7 nm**	**532.05 nm**
Raman shift N_2	283.61 nm	407.48 nm	607.37 nm
Raman shift H_2O	294.65 nm	386.67 nm	660.35 nm
Raman shift O_2	277.51 nm	375.42 nm	580.07 nm

Optical filters exhibit a positive linear temperature coefficient; that is, wavelength increases and decreases with temperature and does so in a linear fashion. As with any other condition under which the filter is to operate, it is important that the operating temperature of the filter be specified. The metal oxide filters used in the LAPS detector are typically designed to operate at 34^{o}C and have a temperature coefficient of 0.0025 nm/^{o}C. Temperature coefficient for alkyl-halide filters (i.e., fluoride) is 0.025

nm/^{o}C. The center wavelength of the filter shifts to shorter wavelengths with increasing angle of the incident radiation and the shift is given by

$$\lambda_i = \lambda_0(n_e^2 - \sin^2 i)^{1/2} / n_e \qquad [4.16]$$

where,

i is the angle of incidence and λ_i is the center wavelength of the filter.

λ_0 is the center wavelength of the filter at normal incidence,

n_e is the effective refractive index of filter.

Off-normal incidence of radiation also results in reduction in peak transmittance and widening of the pass-band. Hence the advanced detector is designed to achieve a highly collimated beam. Half-power bandwidth (HPBW) is the wavelength interval between the relative 50% transmittance points of a band-pass filter and is about 0.15 nm for the visible channels and 0.25 nm for the UV channels for the advanced detector. The in-band transmission is about 20% for the UV channels and close to 50% for the visible channels. Out-of-band transmission is reduced to the order of 10^{-10} at 266 nm and 532 nm, which are the transmitted wavelengths and hence the strongest signals received and to 10^{-6} for the rest of the wavelengths.

4.3 Photomultiplier tubes

The advanced detector system uses the R7400U series manufactured by Hamamatsu for detection of the Raman wavelengths. The advances made in design and development of these PMTs allows for greater flexibility in designing the optical system for the detector. The R7400U is a subminiature photomultiplier tube with a 16-mm diameter and 12-mm sealed length. This PMT can be housed along with the electronics in a 1.6”x 2.5”x 2.5” aluminum box. Comparatively, the LAPS detector PMT housings were much bigger due to the 2-inch diameter PMT used. The smaller size PMTs used in the advanced design leads to shorter optical paths and greater flexibility in positioning the PMTs. The improved design of the R7400U increases photoelectron collection efficiency by over 30% than its predecessors. Fewer stages and shorter path length in the electron pulse results in narrow pulse. Also the lesser number of stages and lower gain results in lower current drain in the pulse thereby permitting higher count rates. The R7400U series PMTs have a pulse width of 1.4 ns yielding higher photon counting rates of 715 MHz, which can be increased by modifications to the PMT. This increases the dynamic range of detection and hence more light can be focused on the PMT active area without saturating the PMT. The quantum efficiency of the 8-mm diameter active area ranges from 11% to 30% over the range of wavelengths used. Figure 4.3 shows the spectral response of the R7400U series PMTs. The R7400U-02 and R7400U-04 will be used for detection in the advanced detector system.

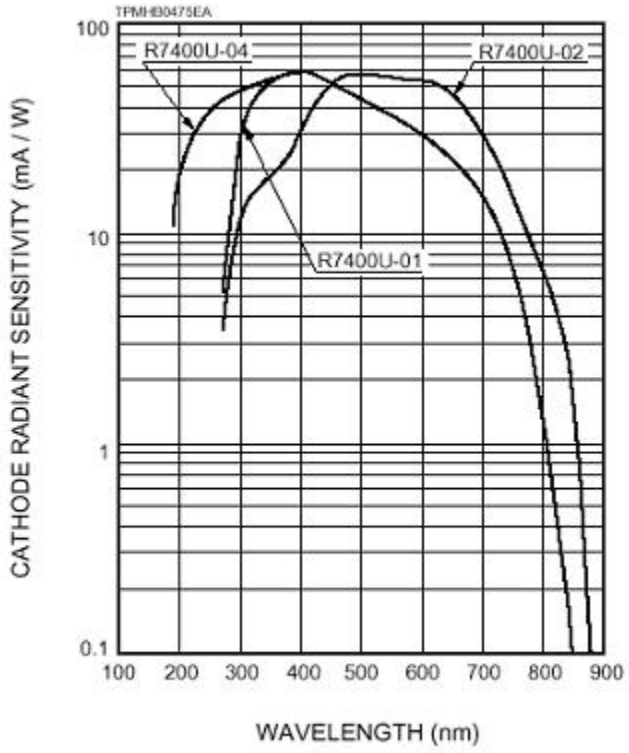

Figure 4.3. Spectral response curves for the R7400U series PMTs [Hamamatsu, 2001]

4.4 Design benefits

The advanced detector is designed to eliminate many of the limitations encountered in the LAPS detector. The new detector is much smaller in size than its predecessor design mainly due to the use of subminiature PMTs. The mechanical design allows the detector box to be rack mountable. A primary concern in the LAPS detector system was the misalignment and vignetting found to be present. The advanced detector is essentially free from misalignment owing to the rigid mounting of the beam splitters. The beam splitters are mounted in a solid aluminum block and are held in position using nylon tipped screws. The beam size is made smaller by using a lens of shorter focal

length. Also, the size of the PMTs and their housing results in reduction in the optical path length. This ensures that a collimated beam is incident on the narrow band-pass filters. The narrow band-pass filters are positioned to maximize the efficiency of the detector. The 660-nm return signal is weakest and is detected first to prevent further reduction in signal strength in the detector. The longer wavelengths are essentially detected first. The shorter wavelengths are detected further along the optical path as they tend to diverge less compared to longer wavelengths. The detector box is mechanically designed to minimize the amount of stray light entering into the system. The beam splitters are oriented exactly at 45 degrees and optical phenomenon such as refraction is compensated for by altering the lateral position of the beam splitters.

Chapter 5

Conclusion

The LAPS instrument, a multi-wavelength Raman lidar, was originally designed as a rugged prototype instrument for the U.S. Navy to obtain RF refractivity measurements. The instrument was used in a number of campaigns and has provided valuable data sets for atmospheric and pollution studies. The ALAPS instrument will be an advanced version of LAPS and it is being developed as an engineering prototype for commercial development of the lidar instrument. The scope of this thesis is limited to the design, simulation and experimental verification of design for an advanced detector to demonstrate the design features considered for the ALAPS instrument. The self-calibration mode in the advanced detector is a major enhancement over the LAPS instrument. Studies comparing use of atmospheric return signal and an external lamp source have concluded that atmospheric light is a better source for calibration and yields lower error levels than an external light source. Data from the advanced detector, which has provision for either mode, would be used to determine an optimal calibration source for the ALAPS instrument.

The advanced detector optical system is designed to accommodate 12.7-mm diameter filters, which would result in cost reduction compared to 25.4-mm diameter filters. It is proposed to develop the advanced detector prototype using 25.4-mm diameter filters and then to progress to 12.7-mm diameter filters after experimental verification of the design from field experiments. The advanced detector incorporates high speed PMTs and faster electronics to provide high-resolution data. Optical filters used for isolation of

Raman wavelengths have a smaller bandwidth, which would yield data with higher SNR. CCDs or detectors can be used at the end of the optical path to provide real time alignment verification of the system. These would essentially record an image of the beam incident on its surface after alignment. Images taken after transportation of the instrument, compared to the original image, detect any misalignments in the optical path without having to open the detector unit. The beam splitter ratios and PMT position are determined to maximize SNR at each wavelength using a lidar measurement-modeling program. The optical components in the advanced detector are rigidly mounted and reduce the extent of realignment required when shifting the instrument. Hence, the new design removes the limitations of the LAPS instrument, discussed in Chapter 2, through optical and mechanical design optimization. The optical systems design is verified using simulations compared with experimental results. Efforts underway to provide an automated fiber-positioning system to maximize return signal, and to capture near field signal will add to the capabilities. Lidar instruments are expected to become the primary source of data for atmospheric studies. The ALAPS system is designed to provide independent, high-resolution profiles of atmospheric properties. It is envisioned that lidar measurements will replace conventional means of profiling the atmosphere for meteorology and other applications in the near future.

References

Balsiger, Franz, Paul T. Haris, and C. Russell Philbrick, "Lower Tropospheric Temperature Measurements Using a Rotational Raman Lidar," Optical Instruments for Weather Forecasting, SPIE Vol. 2832, Denver, CO, pp.53 – 60, Aug. 1996.

Cathodeon Ltd., Deuterium lamps catalog, pp.3, 2001.

Durbin, William, "Lidar Measurements of Ozone in the Lower Atmosphere," Master of Science Thesis for Penn State University, Department of Electrical Engineering, December 1997.

Electron Tubes Inc., On-line data sheets for model numbers: 9893B/350 and 9863B/350, http://www.electrontubes.com, 2001.

Esposito, Steven T., "Applications and Analysis of Raman Lidar Techniques for Measurements of Ozone and Water Vapor in the Troposphere," Master of Science Thesis for Penn State University, Department of Electrical Engineering, May, 1999.

Esposito, Steven T. and C. Russell Philbrick, "Raman/DIAL Technique for Ozone Measurements," Proceedings of the Nineteenth International Laser Radar Conference, NASA Langley Research Center, Hampton, VA, NASA Conf. Publ. 207671, pp. 407 - 410, July 1998.

Fiberguide Industries, Refractive index data sheets of core and cladding material used in all silica fiber, Fax transmission, February 2001.

Harris, P.A.T., "Pure Rotational Raman Lidar for Temperature Measurements in the Lower Troposphere," Ph.D. Dissertation, The Pennsylvania State University, 1995.

Hamamatsu, http://usa.hamamatsu.com/cmp-pdfs/et/R7400U.pdf, April 2000.

Hecht, E., Hecht Optics Second Edition, Boston, MA: Addison-Wesley Publishing Co., 1990.

Jenness, J.R., D.B. Lysak, Jr., and C.R. Philbrick, "Design of a Lidar Receiver with Fiber-Optic Output," Applied Optics Vol. 36, No. 18, pp. 4278 – 4284, 1997.

Li, G., G.S. Chadha, K.R. Mulik, and C.R. Philbrick, "Characterization of Properties of Airborne Particulate Matter from Optical Scattering Using Lidar," Proceedings of the A&WMA Specialty Conference and Exhibition, PM2000: Particulate Matter

and Health, Charleston, South Carolina, January 24-28, 2000, pp. 4ASP1: 8-10.

Measures, Raymond M., Laser Remote Sensing.Wiley-Interscience, New York: 1984.

O'Brien, M.D., T.D. Stevens, and C.R. Philbrick, "Optical Extinction from Raman Lidar Measurements," Optical Instruments for Weather Forecasting, SPIE Proceedings Vol. 2832, pp. 45-52, 1996.

Philbrick, C.R., "Raman Lidar Measurements of Atmospheric Properties," Atmospheric Propagation and Remote Sensing III, SPIE Vol. 2222, 922-931, 1994.

Philbrick, C.R., M.D. O'Brien, D.B. Lysak, T.D. Stevens and F. Balsiger, "Remote sensing by Active and Passive Optical Techniques," AGARD Conference Proceedings, Remote Sensing: A Valuable Source of Information, 582, pp:8-1 – 8-9, October 1996.

Philbrick, C. Russell, "Raman Lidar Capability to Measure Tropospheric Properties," Proceedings of the Nineteenth International Laser Radar Conference, NASA Langley Research Center, Hampton, VA, NASA Conf. Publ. 207671, pp. 289-292, July 1998.

Philbrick, C. Russell and Daniel B.Lysak," Optical Remote Sensing of Atmospheric Properties," Proceedings of the Battlespace Atmospheric and Cloud Impacts on Military Operations Conference, Air Force Research Laboratory, MA, pp.460-467, December 1998

Sherlock, Vanessa, Alain Hauchecome and Jacqueline Lenoble, "Methodology for the independent calibration of Raman backscatter water-vapor lidar systems," Applied Optics Vol. 38, No. 27, pp. 5816 – 5837, September 1999a.

Sherlock, Vanessa, Anne Garnier, Alain Hauchecome and Philippe Keckhut, "Implementation and validation of a Raman lidar measurement of middle and lower tropospheric water vapor," Applied Optics Vol. 38, No. 27, pp. 5838 – 5850, September 1999b.

Appendix

Optical design simulations for the Raman channels in the advanced detector design.

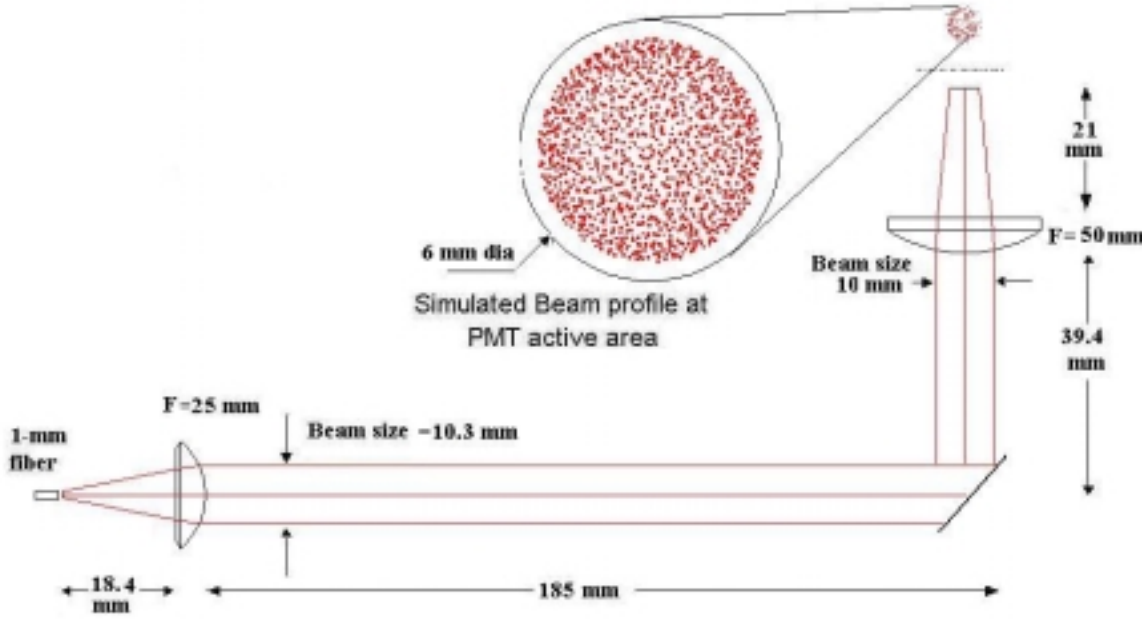

Figure 1. Optical path simulation for 607-nm channel in advanced detector design.

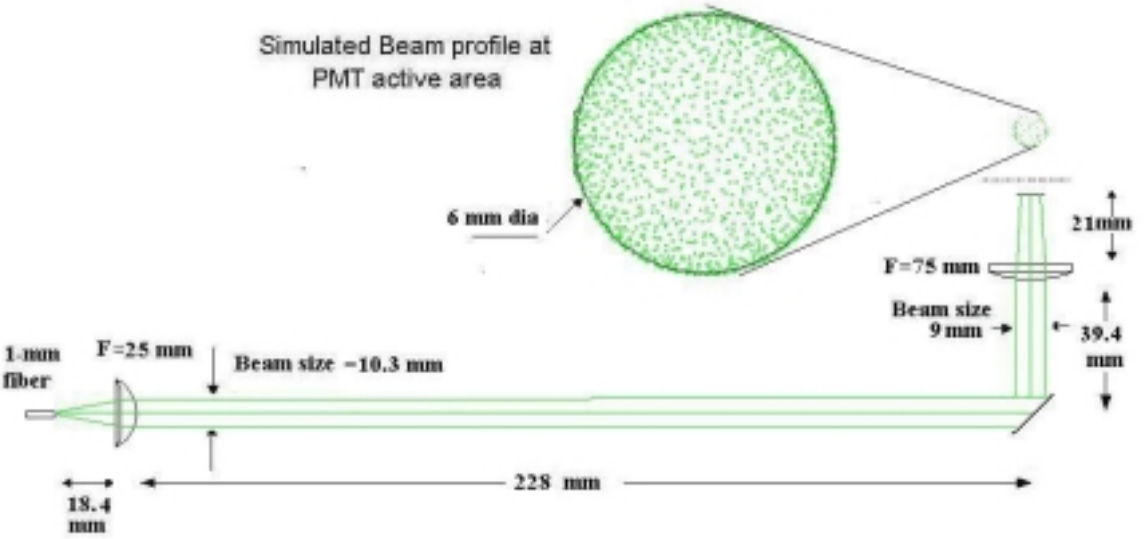

Figure 2. Optical path simulation for 528-nm channel in advanced detector design.

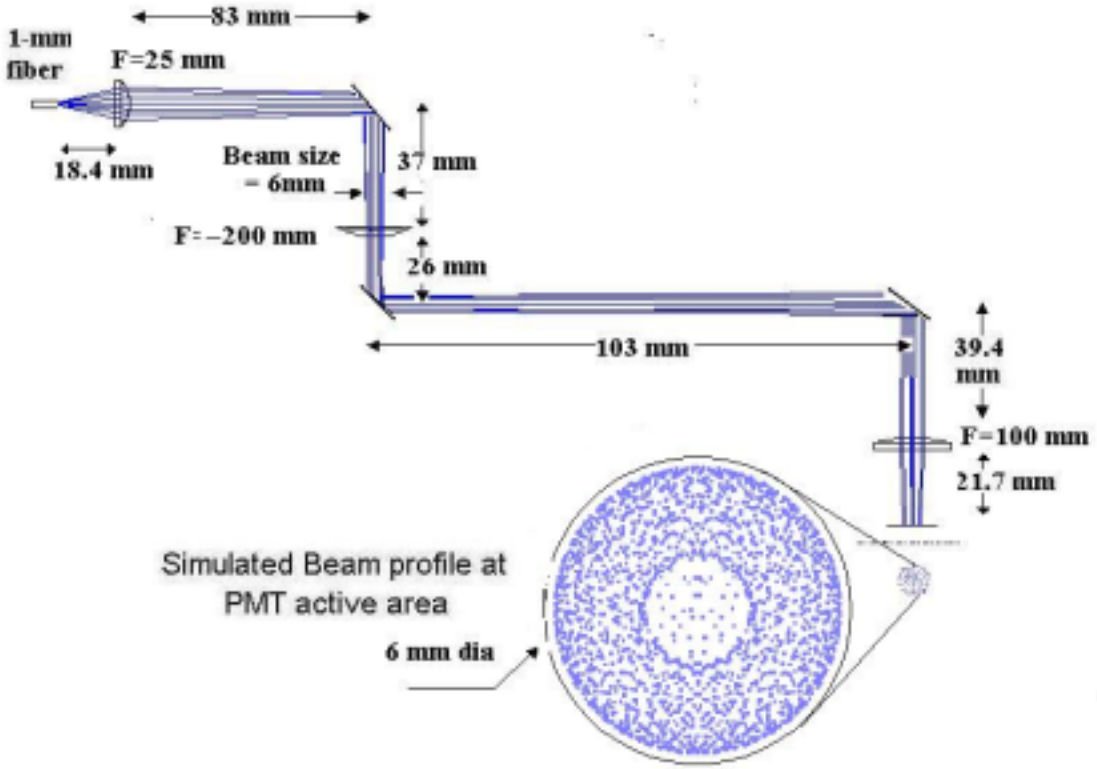

Figure 3. Optical path simulation for 284-nm channel in advanced detector design.

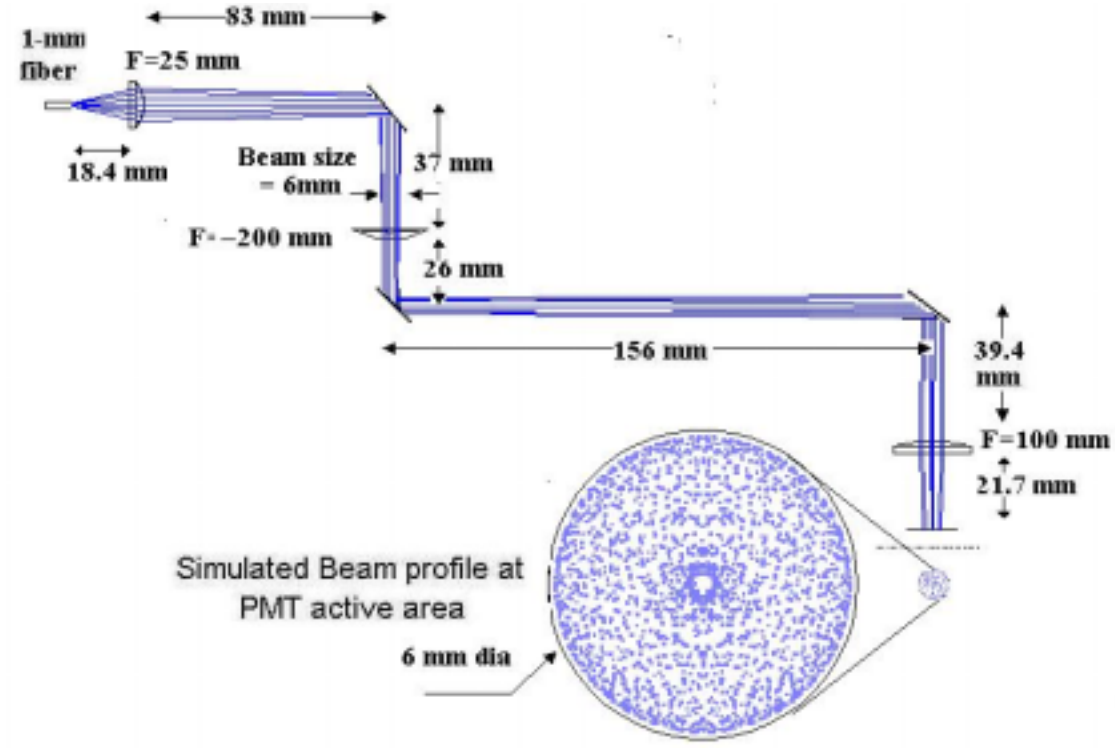

Figure 4. Optical path simulation for 284-nm channel in advanced detector design.

Table 1. Focal length of 25-mm fused-silica plano-convex lens as a function of wavelength

Wavelength λ (nm)	Refractive index for fused silica at wavelength λ	Focal length of plano-convex lens (mm) R=11.5 mm
266	1.49968	23.01
277	1.49453	23.25
295	1.48948	23.49
532	1.46071	24.96
546(design)	1.46008	25.00
607	1.45806	25.10
660	1.45601	25.20

Appendix A

Reference numbers correspond to components as shown in Figure 3.1

Abbreviations	R	Reflect
	T	Transmit
	f	Focal length
	CWL	Center wavelength
	FWHM	Full width half max (bandwidth)

1	Superguide G All–Silica SFS fiber, NA=0.22,1mm dia core
2	Superguide G All–Silica SFS fiber, NA=0.22,1mm dia core
3	Fused Silica plano-convex lens, 25mm f, 12.7mm dia
4	Fused Silica plano-convex lens, 25mm f, 12.7mm dia
5	Beamsplitter R:266, 277,283,294 T:532,528,530,607,660
6	Mirror, UV enhanced aluminum,
7	Beamsplitter R:660 T:532,528,530,607
8	Metal Oxide narrow band filter, CWL=660.35nm FWHM=0.15nm,1” dia
9	BK7 plano-convex lens, 75mm f, 1” dia
10	Beamsplitter R:607 T:532,528,530
11	Metal Oxide narrow band filter, CWL=607.37nm FWHM=0.15nm,1” dia
12	BK7 plano-convex lens, 75mm f, 1” dia
13	Beamsplitter R:30% T:70%
14	Metal Oxide narrow band filter, CWL=528nm FWHM=0.15nm,1” dia
15	BK7 plano-convex lens, 50mm f, 1” dia
16	Beamsplitter R:90% T:10%
17	Metal Oxide narrow band filter, CWL=530nm FWHM=0.15nm,1” dia
18	BK7 plano-convex lens, 50mm f, 1” dia
19	Beamsplitter R:50% T:50%
20	Metal Oxide narrow band filter, CWL=532nm FWHM=0.15nm,1” dia
21	BK7 plano-convex lens, 50mm f, 1” dia
22	Mirror, UV enhanced aluminum,
23	Beamsplitter R:294 T:266,283,277

24	Metal Oxide narrow band filter,CWL=294.65nm FWHM=0.25nm,1” dia
25	Fused Silica plano-convex lens, 75mm f, 1” dia
26	Beamsplitter R:283 T:266, 277
27	Metal Oxide narrow band filter, CWL=283.61nm FWHM=0.25nm,1” dia
28	Fused Silica plano-convex lens, 100mm f, 1” dia
29	Beamsplitter R:277 T:266
30	Metal Oxide narrow band filter, CWL=277.51nm FWHM=0.25nm, 1” dia
31	Fused Silica plano-convex lens, 100mm f, 1” dia
32	Beamsplitter R: 50% T:50%
33	Metal Oxide narrow band filter, CWL=266.025nm FWHM=0.25nm, 1” dia
34	Fused Silica plano-convex lens, 100mm f, 1” dia
35	Filter wheel, containing filters: 8, 11,17,24,27,30
36	Fused Silica plano-convex lens, 75mm f, 1” dia